

Effect of Nitroxoline on Angiogenesis and Growth of Human Bladder Cancer

Joong Sup Shim, Yoshiyuki Matsui, Shridhar Bhat, Benjamin A. Nacev, Jing Xu, Hyo-eun C. Bhang, Surajit Dhara, Kee Chung Han, Curtis R. Chong, Martin G. Pomper, Alan So, Jun O. Liu

Manuscript received March 21, 2010; revised October 14, 2010; accepted December 15, 2010.

Correspondence to: Jun O. Liu, PhD, Department of Pharmacology and Molecular Sciences, Johns Hopkins School of Medicine, 725 N Wolfe St, Hunterian Building 516, Baltimore, MD 21205 (e-mail: joliu@jhu.edu).

Background Angiogenesis plays an important role in tumor growth and metastasis; therefore, inhibition of angiogenesis is a promising strategy for developing new anticancer drugs. Type 2 methionine aminopeptidase (MetAP2) protein is likely a molecular target of angiogenesis inhibitors.

Methods Nitroxoline, an antibiotic used to treat urinary tract infections, was identified from a high-throughput screen of a library of 175 000 compounds for MetAP2 inhibitors and from a parallel screen using the Johns Hopkins Drug Library to identify currently used clinical drugs that can also inhibit human umbilical vein endothelial cells (HUVEC) proliferation. To investigate the mechanism of action of nitroxoline, inhibition of MetAP2 activity and induction of senescence were assessed in HUVEC. To test the antiangiogenic activity of nitroxoline, endothelial tube formation in Matrigel and microvessel formation in Matrigel plugs *in vivo* were assessed. Antitumor efficacy of nitroxoline was evaluated in mouse models of human breast cancer xenograft ($n = 10$) and bladder cancer orthotopic xenograft ($n = 11$). Furthermore, the mechanism of action of nitroxoline was investigated *in vivo*.

Results Nitroxoline inhibited MetAP2 activity *in vitro* (half maximal inhibitory concentration [IC_{50}] = 54.8 nM, 95% confidence interval [CI] = 22.6 to 132.8 nM) and HUVEC proliferation ($IC_{50} = 1.9 \mu\text{M}$, 95% CI = 1.54 to 2.39 μM). Nitroxoline inhibited MetAP2 activity in HUVEC in a dose-dependent manner and induced premature senescence in a biphasic manner. Nitroxoline inhibited endothelial tube formation in Matrigel and reduced microvessel density *in vivo*. Mice (five per group) treated with nitroxoline showed a 60% reduction in tumor volume in breast cancer xenografts (tumor volume on day 30, vehicle vs nitroxoline, mean = 215.4 vs 86.5 mm^3 , difference = 128.9 mm^3 , 95% CI = 32.9 to 225.0 mm^3 , $P = .012$) and statistically significantly inhibited growth of bladder cancer in an orthotopic mouse model (tumor bioluminescence intensities of vehicle [$n = 5$] vs nitroxoline [$n = 6$], $P = .045$).

Conclusion Nitroxoline shows promise as a potential therapeutic antiangiogenic agent.

J Natl Cancer Inst 2010;102:1855–1873

Angiogenesis plays an important role in the development and pathogenesis of many human diseases, including cancer and rheumatoid arthritis (1–3). It requires endothelial cell proliferation, invasion across the basement membrane surrounding the existing blood vessel and differentiation to form capillary structures [reviewed in (4)]. The role of angiogenesis in tumor growth and metastasis is well established, since Judah Folkman's discovery of this process in the early 1970s [reviewed in (5)]. Inhibition of angiogenesis has become a promising strategy to slow the growth of tumors and to enhance the efficacy of cytotoxic anticancer drugs (6,7).

The fumagillin family of natural products is among the most potent small-molecule inhibitors of angiogenesis known to date, based on *in vitro* and preclinical studies (8). A synthetic analog of fumagillin, known as TNP-470, was tested in phase I–II clinical

trials for various cancers including Kaposi sarcoma, renal cell carcinoma, brain cancer, breast cancer, cervical cancer, and prostate cancer [reviewed in (9)]. However, its *in vivo* instability and dose-limiting toxicity prevented TNP-470 from further clinical development (10–12). In an attempt to elucidate the molecular mechanism of inhibition of angiogenesis by fumagillin and TNP-470, we and others identified the type 2 methionine aminopeptidase (MetAP2) protein as the likely molecular target of these small-molecule angiogenesis inhibitors (13,14). MetAP2 is one of the three known enzymes that catalyses the removal of N-terminal initiator methionine from nascent polypeptides during protein synthesis in mammalian cells [reviewed in (15)]. Inhibition of MetAP2 by TNP-470 and other inhibitors leads to the activation of tumor protein p53 (TP53), a tumor suppressor, and the accompanying

CONTEXT AND CAVEATS

Prior knowledge

Angiogenesis, or the proliferation, migration, and invasion of endothelial cells to form capillaries, has an important role in tumor growth and metastasis. The type 2 methionine aminopeptidase (MetAP2) protein is a potential antiangiogenic target.

Study design

A library of 175 000 compounds was screened for MetAP2 inhibitors, and the Johns Hopkins Drug Library (JHDL) was screened for endothelial cell proliferation inhibitors among the currently used clinical drugs. Nitroxoline, an antibiotic used in many countries to treat urinary tract infection, was the common potential hit from both screens. The drug was tested for antiangiogenic activity in endothelial cells and in mice, and anticancer activity was assessed in mouse models of human breast cancer and orthotopic bladder cancer xenografts.

Contribution

Nitroxoline inhibited MetAP2 activity and endothelial cell proliferation. It also inhibited angiogenesis both *in vitro* and *in vivo*. Tumor volume was reduced by 60% in breast cancer xenografts. Tumor growth and area were also statistically significantly reduced in bladder cancer xenografts.

Implications

Nitroxoline has the potential for clinical use as an effective antiangiogenesis agent.

Limitations

The results in mouse models may not be predictive of clinical gains in humans. Also, a dose optimization was not done and the results in mice were obtained from a single dose.

From the Editors

increased expression of cyclin-dependent kinase inhibitor 1A (CDKN1A; also known as p21) that inhibits cyclin E1 (CCNE1) and cyclin-dependent kinase 2 (CDK2) complex required for the phosphorylation of retinoblastoma 1 (RB1) and G1-S cell cycle transition in endothelial cells (16,17). Given its unique function in endothelial cell proliferation, MetAP2 has served as a target for discovering and developing novel antiangiogenic agents (18,19).

Unlike MetAP2, which is involved in co-translational modification of proteins, the silent information regulator 2 (SIR2) family of nicotinamide adenine dinucleotide (NAD)-dependent deacetylases (also known as sirtuins [SIRTs]) have been shown to play important roles in gene silencing and DNA repair, among other cellular processes [reviewed in (20)]. There are seven human sirtuins (SIRT1–7), and each isoform shows a distinct substrate specificity and subcellular localization (21,22). The SIRT1 protein is located in the nucleus and targets a variety of acetylated substrates including TP53 (23). There is accumulating evidence that SIRT1 plays an important role in cellular senescence and angiogenesis [reviewed in (24)]. Inhibition of SIRT1 activity is sufficient to induce premature senescence in endothelial cells and inhibit angiogenesis *in vivo* (25,26), which makes SIRT1 another promising target for discovering new inhibitors of angiogenesis.

Although the conventional drug development process that involves *de novo* discovery and refinement of inhibitors of individually validated targets such as VEGF or MetAP2 represents an effective approach to develop novel antiangiogenic drugs, it is a costly and time-consuming process (27). A complementary approach that allows a dramatic acceleration of the development of new drugs is to screen existing drugs for previously unknown antiangiogenic activity [reviewed in (28)]. Because existing drugs, with favorable pharmacokinetic and pharmacodynamic properties and tolerable side effects, are already used in humans for different indications, such newly discovered agents can quickly enter human clinical efficacy studies using the existing drug administration regimen. For this purpose, we recently assembled a library of mostly Food and Drug Administration–approved drugs, dubbed the Johns Hopkins Drug Library (JHDL), containing a total of 2687 clinical drugs, and screened it in a variety of biological assays including screening for antimalarial drugs and inhibitors of hypoxia-inducible factor-1 α (HIF1A) (29,30). Several promising agents were identified from the JHDL, including the antimalarial drug astemizole (29) and cardiac glycosides as novel inhibitors and HIF1A-dependent transcription of genes that are important for angiogenesis and tumor growth (30). Astemizole and cardiac glycosides were subsequently shown to be efficacious in animal models of malaria infection and HIF1A-dependent tumor growth, respectively, underscoring the power to use JHDL to discover clinically feasible drugs with desired pharmacological activities.

In this study, we used two parallel screens—a target-based screen using MetAP2 against a library of 175 000 chemical compounds (31), and a cell-based screen using human endothelial cells against JHDL—to identify novel MetAP2 inhibitors with clinically feasible antiangiogenic activity. The primary hits from both screens were subsequently validated by determining the half maximal inhibitory concentration (IC₅₀) values for inhibition of either MetAP2 activity or endothelial cell proliferation. Here, we focused on nitroxoline, which was identified as a hit in both screens and is an antibiotic used in humans to treat urinary tract infections. We elucidated its unique mode of action in human endothelial cells and tested it for antiangiogenic activity in mouse xenograft models.

Materials and Methods

Cell Lines and Cell Culture

Human umbilical vein endothelial cells (HUVEC) (Lonza, Allendale, NJ) were grown in endothelial cell growth medium-2 (EGM-2) using the EGM-2 bullet kit (Lonza) per manufacturer's instructions. HUVEC phenotype was verified by morphological observation throughout serial passage by the manufacturer. HCC1954 human breast cancer cells (kindly provided by Dr Bert Vogelstein, Johns Hopkins University School of Medicine, Baltimore, MD) were grown in Roswell Park Memorial Institute (RPMI)-1640 medium (Invitrogen, Carlsbad, CA), supplemented with 10% fetal bovine serum (FBS) (Invitrogen). The genotype of the cell line was verified using the short tandem repeat profiling by Genetic Resources Core Facility (Johns Hopkins University School of Medicine). The cells were maintained in a humidified incubator at 37°C adjusted to 5% CO₂. The human bladder cancer cell line, KU7 was grown in Dulbecco's Modified Eagle's Medium

(DMEM) containing 5% FBS and the genotype was verified as described previously (32). To generate KU7 luciferase reporter cell line (KU7-luc), KU7 cells were infected with a lentivirus containing the firefly luciferase gene (25 μ L viral supernatant/mL medium) mixed with polybrene (4 μ g/mL medium) as described previously (32). High Five (BTI-TN-5B1-4) cells (Invitrogen) were grown in Grace insect cell medium (Invitrogen) and were maintained in a nonhumidified incubator at 27°C as per manufacturer's instructions.

Monoclonal and Polyclonal Antibodies

Mouse anti-human methionine on 14-3-3 γ (Met-14-3-3 γ) monoclonal antibody (mAb) (clone HS23) was purchased from Novus Biologicals (Littleton, CO). Rabbit anti-human acetyl-TP53 (acetyl-K382) mAb (clone EPR358[2]) was purchased from Abcam (Cambridge, MA). Mouse anti-sea urchin acetyl-tubulin, alpha 1a (Ac-TUBA1A) mAb (clone 6-11B-1, binds to human proteins) was purchased from Sigma-Aldrich (St Louis, MO). Mouse anti-human MetAP2 mAb was generated as described previously (33). Mouse anti-human CD31 (also known as platelet-endothelial cell adhesion molecule 1 [PECAM1]) mAb was purchased from BD Pharmingen (San Jose, CA). The following primary and secondary antibodies were purchased from Santa Cruz Biotechnology (Santa Cruz, CA): mouse anti-human TP53 mAb, rabbit anti-human Pan-14-3-3, rabbit anti-human p21, mouse anti-human RB1 mAb, mouse anti-human TUBA1A, goat anti-human glyceraldehyde 3-phosphate dehydrogenase (GAPDH), mouse anti-human SIRT1, rabbit anti-human acetyl-histone H3 (H3F3A), rabbit anti-human acetyl-histone H4 (H4F3) (acetyl-K16), rabbit anti-human histone H3, normal mouse immunoglobulin G (IgG), and horseradish peroxidase (HRP)-conjugated anti-mouse or anti-rabbit IgG.

Purification of MetAP2 Enzyme

Recombinant human MetAP2 enzyme was prepared using histidine (His)-tagged MetAP2 as described previously (34). His-tagged human MetAP2 was expressed by using the Bac-to-Bac baculovirus expression system (Invitrogen). Recombinant baculovirus were generated and amplified in High Five (BTI-TN-5B1-4) cells per manufacturer's instructions. High Five (BTI-TN-5B1-4) cells were harvested 36 hours after baculovirus infection. The cell pellet was weighed and lysed (5 mL/g of wet pellet) in prechilled lysis buffer (10 mM HEPES [pH 8.0], 100 mM KCl, 1.5 mM MgCl₂, 10% glycerol, 1% Nonidet P-40, 1 mM phenylmethylsulfonyl fluoride [PMSF], 2 mg/mL leupeptin, 2 mg/mL aprotinin, 1 mg/mL pepstatin). The lysate was incubated on ice for 10 minutes and centrifuged at 10000g for 10 minutes. The supernatant was diluted in buffer A (10 mM HEPES [pH 8.0], 100 mM KCl, 1.5 mM MgCl₂, 10% glycerol) and incubated for 1 hour at 4°C with 1 mL of pre-equilibrated Talon resin (Clontech, Mountain View, CA). The Talon resin was washed four times with buffer A and was transferred as a slurry into a Bio-Rad Econo column (Bio-Rad, Hercules, CA). The 6 \times His-tagged MetAP2 was eluted with 50 mM imidazole in buffer A, and fractions were collected. The amount and purity of recombinant MetAP2 were analyzed by measuring the absorbance at 280 nm by Ultrospec 2100 spectrophotometer (GE Healthcare, Pittsburgh, PA) and sodium dodecyl sulfate-polyacrylamide gel electrophoresis (SDS-PAGE).

High-throughput Screening for MetAP2 Inhibitors

A chemical library was constructed with 175 000 compounds that were provided by ASDI, Inc (Newark, DE) or purchased from Maybridge (Trevillet, UK), Bionet (Cornwall, UK), and Sigma-Aldrich. The compounds were dissolved in 100% dimethyl sulfoxide (DMSO), and stored at 20°C, as described previously (31). Compounds arrayed in 384-well plate (Nunc, Roskilde, Denmark), at 10 μ M final concentration, were screened using the MAP-C2 microplate processor (Titertek, Huntsville, AL) for dispensing reagents, and a microplate reader (BMG Labtech, Offenburg, Germany) for data collection. MetAP2 was incubated with test compounds in 45 μ L assay buffer (20 mM HEPES [pH 7.5], 40 mM KCl, and 10 μ M MnCl₂) at room temperature for 20 minutes. The enzymatic reaction was initiated by addition of 5 μ L of 6 mM methionylprolyl-*p*-nitroanilide (Met-Pro-*p*NA) in assay buffer together with 0.005 units of proline aminopeptidase as described previously (35). Absorbance at 405 nm was recorded at 30 minutes. The percentage of net decrease in the absorbance in comparison with control wells with solvent carrier was taken as the percentage of inhibition by a given compound tested. Compounds that exhibited more than 50% inhibition were selected for further screening; this cutoff value was based on many published articles (29–31). The preliminary hits were rescreened at three different concentrations (30, 10, and 3 μ M), and the relative potency was compared and used to rank the hits. The IC₅₀ value of nitroxoline was determined using six different concentrations (0.5, 5, 50, 500, 5000, and 50000 nM) of nitroxoline in four independent experiments.

Cell-Based Screening for Inhibitors of Proliferation and ³H-thymidine Incorporation Assay

For the screening of drugs that inhibited HUVEC proliferation, 10 mM stock solutions of the JHDL were arrayed in 96-well plates, and a final concentration of 10 μ M was used for the screening. HUVEC (5000 cells per well) were seeded in 96-well plates containing 0.2 mL of EGM-2 medium and allowed to adhere at 37°C for 24 hours. The cells were then treated with 10 μ M of each drug from the JHDL for 24 hours. Cells were pulsed with 1 μ Ci ³H-thymidine (6.7 Ci per m mol) (MP Biomedicals, Solon, OH) for 8 hours, and then treated with 1 \times trypsin-EDTA (Invitrogen). The suspended cells were harvested onto FilterMat A glass fiber filters (Wallac, Turku, Finland) using the Harvester 96 cell harvester (Tomtec, Hamden, CT), and ³H-thymidine counts were determined using a MicroBeta plate reader (Perkin Elmer, Waltham, MA). The IC₅₀ value of nitroxoline was determined using six different concentrations (0.1, 0.5, 1, 5, 10, and 50 μ M) from four independent experiments.

Transfection of HUVEC with small-interfering RNAs (siRNAs) against MetAP2 and SIRT1

Duplex oligonucleotides encoding siRNA against human MetAP2 (product number SI00092288), two SIRT1 siRNAs targeting different sites in SIRT1 mRNA (product numbers SI00098434 for siRNA1 and SI00098448 for siRNA3), and a negative control siRNA were purchased from Qiagen (Valencia, CA). The siRNA sequences were as follows:

MetAP2 siRNA: 5'-GACUGUUCACGCAAGUUAATT-3'

SIRT1 siRNA1 (SI00098434): 5'-AGCGAUGUUUGAUUUGAATT-3'

SIRT1 siRNA3 (SI00098448): 5'-GGGUCUCCCCUCAA GUAATT-3'

Control siRNA: 5'-UUCUCCGAACGUGUCACGUTT-3'.

On the day of transfection, HUVEC were seeded in a 6-well plate (3×10^5 cells per well) and were transfected with either MetAP2 (5, 10, and 20 nM) or SIRT1 (5, 10, and 50 nM) siRNA using HiperFect transfection reagent (Qiagen) per manufacturer's instructions. Forty-eight hours after transfection, the cell lysates were prepared for immunoblot analysis.

Immunoblot

Cell lysates were prepared by adding 150 μ L (per well in 6-well plate) of 2 \times Laemmli buffer (4% SDS, 20% glycerol, 10% 2-mercaptoethanol, 0.004% bromophenol blue, 0.125 M Tris-HCl [pH 6.8]) and boiled for 5 minutes. Lysates containing equal amounts of proteins were separated by SDS-PAGE and transferred to nitrocellulose membranes (0.45 μ m pore size; Bio-Rad, Hercules, CA). Membranes were incubated in a blocking solution containing 5% nonfat dry milk at room temperature for 1 hour. Membranes were incubated at 4°C overnight with the primary antibodies—mouse anti-human TP53 (dilution, 1:2000), mouse anti-human Met-14-3-3 γ (dilution, 1:1000), rabbit anti-human Pan-14-3-3 (dilution, 1:1000), rabbit anti-human p21 (dilution, 1:500), mouse anti-human RB1 (dilution, 1:1000) mouse anti-human MetAP2 (dilution, 1:2000), mouse anti-human TUBA1A (dilution, 1:2000), goat anti-human GAPDH (dilution, 1:1000), mouse anti-human SIRT1 (dilution, 1:2000), rabbit anti-human acetyl-TP53 (acetyl-K382) (dilution, 1:500), mouse anti-sea urchin acetyl-TUBA1A (dilution, 1:2000), rabbit anti-human acetyl-histone H3 (dilution, 1:1000), rabbit anti-human acetyl-histone H4 (acetyl-K16) (dilution, 1:1000), rabbit anti-human histone H3 (dilution, 1:1000), followed by incubation with HRP-conjugated anti-mouse (dilution, 1:2000) or anti-rabbit (dilution, 1:2000) IgG at room temperature for 1 hour. Antibody-protein complexes were detected using enhanced chemiluminescence (ECL) immunoblotting detection reagent (GE Healthcare). The immunoblot signals were quantified using Image J software (<http://rsbweb.nih.gov/ij/>). All experiments were performed three independent times.

Reverse Transcriptase–Polymerase Chain Reaction (RT-PCR)

HUVEC (5×10^5 cells) were seeded in 100-mm tissue culture dishes and grown for 24 hours. Cells were treated with DMSO, nitroxoline (5 μ M) or TNP-470 (10 nM) for 24, 48, or 72 hours. Total RNA was isolated using Trizol reagent (Invitrogen), per manufacturer's instructions. The RNA (5 μ g) was then reverse transcribed into cDNA using Superscript III (Invitrogen). The cDNA product was amplified by PCR using the following conditions: 94°C, 4 minutes; 94°C, 30 seconds; 60°C, 30 seconds; 72°C, 40 seconds, and an additional 28 cycles; 72°C, 10 minutes.

The following primers were used:

TP53 forward: 5'-CCCCTCCTGGCCCCTGTCATCTTC-3'

TP53 reverse: 5'-GCAGCG CCTCACAACCTCCGTCAT-3'

p21 forward: 5'-GAGGCCGGGATGAGTTGGGA GGAG-3'

p21 reverse: 5'-CAGCCGGCGTTTGGAGTGGTAGAA-3'.

Results for TP53 and p21 band intensities were normalized to GAPDH band intensity. The experiment was performed three independent times.

Senescence-Associated β -Galactosidase (SA- β -gal) Assay

HUVEC were seeded in a 6-well plate (1×10^4 cells per well) and were grown at 37°C for 24 hours. Cells were treated with various concentrations of nitroxoline (1, 2, 5, and 10 μ M) and 10 nM TNP-470 for 3–5 days. Treatment with valproic acid (0.1 mM), a histone deacetylase inhibitor, was used as a positive control for induction of HUVEC senescence. Cells were then washed with phosphate-buffered saline (PBS; pH 7.4) containing 137 mM NaCl, 2.7 mM KCl, 8 mM Na₂HPO₄, and 2 mM KH₂PO₄ (Invitrogen) and fixed with a fixative containing 2% formaldehyde and 0.2% glutaraldehyde in PBS at room temperature for 10 minutes. Cells were washed twice with PBS and were incubated in freshly prepared SA- β -gal staining solution (1 mg/mL 5-bromo-4-chloro-3-indolyl β -D-galactopyranoside [X-gal], 5 mM potassium ferrocyanide, 5 mM potassium ferricyanide, 150 mM NaCl, 2 mM MgCl₂, and 40 mM citric acid titrated with NaH₂PO₄ [pH 6.0]) at 37°C for 24 hours, without CO₂ and protected from light. The SA- β -gal solution was removed and the cells were washed twice with PBS before they were observed under a Nikon Eclipse TS100 microscope (Nikon Corp., Tokyo, Japan) for a medium- to dark-blue staining, indicative of SA- β -gal activity.

Expression and Purification of Recombinant SIRT1

Flag-tagged full-length *SIRT1* gene (Addgene plasmid 1791: Flag-SIRT1) was constructed by the laboratory of Michael E. Greenberg and was obtained through Addgene (Cambridge, MA) (36). The gene was subcloned into the glutathione *S*-transferase (GST)-tagged pGEX-6P-2 vector (GE Healthcare) at *Bam*HI and *Not*I sites using the following primers (the restriction enzyme recognition sites are underlined):

SIRT1 forward: 5'-ATAGGATCCATGGCGGACGAGGC-3'

SIRT1 reverse: 5'-ATAGCGGCCCGCCTATGATTTGTTT GATGGATAG-3'.

The GST-SIRT1 construct was amplified using DH5 α competent cells (Invitrogen) and the purified clone was introduced to BL21 competent cells (EMD4Biosciences, San Diego, CA) for expression. The GST-SIRT1-transformed BL21 cells were grown in 1 L of Luria-Bertani (LB) media containing 10 g trypton (BD Biosciences, San Jose, CA), 5 g yeast extract (BD Biosciences), and 10 g NaCl in the presence of 50 μ g/mL ampicillin (American Bioanalytical, Natick, MA) at 37°C to reach optical density of 0.8 at 600 nm measured by Ultrospec 2100 spectrophotometer. The GST-SIRT1 expression was induced by incubating the BL21 with 0.5 mM isopropyl β -D-thiogalactopyranoside (American Bioanalytical) at 37°C for 3 hours. The BL21 cells were then centrifuged at 4000g at 4°C for 10 minutes. The cell pellets were resuspended and lysed in 50 mL of the lysis buffer containing 2 mM EDTA, 0.1% β -mercaptoethanol, 15 μ g/mL leupeptin, 10 μ g/mL aprotinin, 1 mM PMSF, 1 mg/mL lysozyme (American Bioanalytical) and 1% Triton X-100 in PBS. The lysates were centrifuged at 26900g at 4°C for 20 minutes. Two milliliter bed volume of glutathione beads (GE Healthcare) was added to the cell lysates and incubated with rotation at 4°C for 2 hours. The beads

were then centrifuged at 330g at 4°C for 5 minutes, washed twice with PBS, resuspended in 5 mL PBS, and transferred to a disposable polypropylene column (Pierce, Rockford, IL). The GST-tag was removed by adding PreScission Protease (GE Healthcare) into the column and incubating at 4°C overnight with rotation. The supernatant containing purified SIRT1 was concentrated using the Vivaspin 6 (GE Healthcare), and the protein concentration was measured using the Bio-Rad Protein Assay kit (Bio-Rad).

Measurement of Sirtuin Activity

Immunoblot Assay to Detect Sirtuin Activity. To analyze sirtuin activity in HUVEC, we measured the levels of acetylated sirtuin substrates by immunoblot. HUVEC were seeded in 6-well plates (2×10^5 cells per well) and grown for 24 hours. Cells were treated with various compounds including nitroxoline (0.5–20 μ M), sirtinol (30 μ M), trichostatin A (TSA; 0.3 μ M), EX527 (0.5–20 μ M), and TNP-470 (10 nM) for either a short (6 hours) or long (20–24 hours) duration. Sirtinol, a plant SIR2 inhibitor, was used as a positive control to detect an increase in the level of acetylated histone H3 (37). Treatment with TSA, a class-I and -II histone deacetylase (HDAC) inhibitor (38), was used as a positive control to detect an increase in the level of acetylated TP53 (acetyl-K382). EX527, a mammalian SIRT1 inhibitor, was used as a positive control for inhibiting SIRT1 activity (39). We used two different time points for this assay because the acetylation of proteins is reversible and TSA is known to increase the acetylation of HDAC substrate proteins temporarily (40). The acetylation level of TP53 at K382 was assessed to determine SIRT1 and HDAC activities in HUVEC. The acetylation level of TUBA1A was analyzed for SIRT2 activity and the acetylation level of histone H3 was analyzed to determine SIRT2 and HDAC activity. The levels of acetylated TP53, TUBA1A, and histone H3 were measured by incubation with the following primary antibodies—rabbit anti-human acetyl-TP53 (acetyl-K382) (dilution, 1:500), mouse anti-sea urchin acetyl-TUBA1A (dilution, 1:2000), and rabbit anti-human acetyl-histone H3 (dilution, 1:1000) at 4°C overnight, followed by incubation with HRP-conjugated anti-mouse (dilution, 1:2000) or anti-rabbit (dilution, 1:2000) IgG at room temperature for 1 hour. Bound antibodies were detected using ECL as described earlier. The immunoblot signals were quantified using Image J software. The acetylated TP53 (acetyl-K382) levels were normalized to total TP53 protein levels and their relative differences with the corresponding controls were calculated by dividing the level of acetylated TP53 (acetyl-K382) of the test sample by the level of acetylated TP53 (acetyl-K382) of the control sample. The acetylated TUBA1A and histone H3 levels were normalized to their respective total protein levels, and their relative differences with the corresponding controls were calculated by dividing the level of acetylated TUBA1A or histone H3 of the test sample by the level of acetylated TUBA1A or histone H3 of the control sample. All experiments were performed three independent times.

Dot Blot Assay to Detect Sirtuin Activity. For SIRT1 assays, purified recombinant SIRT1 protein (0.3 μ M) was incubated with various concentrations of nitroxoline (0.5–50 μ M) in 20 μ L assay buffer (50 mM Tris-HCl [pH 8.0], 137 mM NaCl, 2.7 mM KCl, 1 mM $MgCl_2$, and 1 mg/mL bovine serum albumin) (Enzo Life

Sciences, Plymouth Meeting, PA) at 37°C for 2 hours. The TP53 acetyl (K382) peptide (100 μ g/mL) (Abcam) and nicotinamide adenine dinucleotide (NAD; 100 μ M) (Enzo Life Sciences) were added to the solution and incubated at 37°C for 1 hour. After incubation, a small aliquot (2 μ L) of reaction solution was dot-blotted onto a nitrocellulose membrane of 0.45 μ m pore size (Bio-Rad). The membrane was then blocked in a blocking buffer containing 5% bovine serum albumin in Tris-buffered saline Tween-20 (TBS-T) (20 mM Tris-HCl [pH 7.5], 150 mM NaCl, 0.05% Tween-20) at room temperature for 1 hour. The acetylated peptide was probed with rabbit anti-human acetyl-TP53 (acetyl-K382) antibody (dilution, 1:500 in blocking buffer) at room temperature for 1 hour. After washing three times with TBS-T, the membrane was incubated with HRP-conjugated anti-rabbit IgG (dilution, 1:2000) at room temperature for 30 minutes. The antibody signal was then detected using ECL reagent. For SIRT2 and SIRT3 (Enzo Life Sciences) assays, an enzyme concentration of 0.05 unit/ μ L was used. All procedures were the same as that for SIRT1 measurement, except the acetylated histone H4 (acetyl-K16) peptide (Abcam) was used as a substrate. Rabbit anti-human acetyl-histone H4 (acetyl-K16) antibody (dilution, 1:1000) was used to detect the acetylated histone H4 peptides. The resulting dot blot signals were quantified using Image J software and the data were plotted using GraphPad Prism 4.0 software (GraphPad Software, Inc, San Diego, CA). All experiments were performed three independent times.

Combination Index Analysis

The synergistic activity between two drugs in inhibiting HUVEC proliferation was calculated mathematically based on Chou-Talalay combination index equation (41). To determine whether the combination of EX527 and TNP-470 was synergistic, additive, or antagonist, we used the CompuSyn software (ComboSyn, Paramus, NJ) that allows the calculation of the combination index based on the algorithm of Chou-Talalay method. Combination index values less than 1 indicate synergism, values equal to 1 indicate an additive effect, whereas values greater than 1 indicate antagonism. Because the potency of EX527 and TNP-470 on HUVEC proliferation was different, the concentrations of the drug combinations were decided based on IC_{50} values of each drug. We chose four combinations of the two drugs with a fixed concentration ratio as follows—combination of 1 IC_{50} for both EX527 and TNP-470; combination of 1/2 IC_{50} for both EX527 and TNP-470; combination of 1/4 IC_{50} for both EX527 and TNP-470; and combination of 1/8 IC_{50} for both EX527 and TNP-470. The effect of drug combinations on HUVEC proliferation was tested using the 3H -thymidine incorporation assay. The resulting data were analyzed to calculate the combination index, and results were plotted as the mean (95% confidence interval [CI]) values from three independent experiments. To see how substantial the synergism was, the statistical significance of the difference of each combination index value from 1 (combination index = 1, additive effect) was analyzed by one-sample *t* test (two-sided) when the theoretical mean was equal to 1.

Endothelial Cell Tube Formation Assay

The tube formation assay, a model for assessment of angiogenesis, was conducted as described previously (42) with minor modifications.

A 96-well plate was coated with Matrigel (BD Biosciences) by adding 50 μ l of ice-cold Matrigel solution per well followed by incubating at 37°C for 1 hour. HUVEC were then seeded on the Matrigel-coated wells (2×10^4 cells per well). Cells were treated with nitroxoline (5 and 10 μ M), EX527 (1 μ M), TNP-470 (10 nM), or the combination of EX527 (1 μ M) and TNP-470 (10 nM). Cells were then incubated in a humidified 5% CO₂ incubator at 37°C for 16–18 hours. The cells were washed carefully with PBS once, and Calcein-AM (BD Biosciences) solution in PBS (final concentration 2 μ M) was added. After incubation at 37°C for an additional 30 minutes, the cells were washed carefully with PBS and the fluorescence-labeled endothelial cell tubes were observed under the Nikon Eclipse TS100 fluorescence microscope (485-nm excitation and 520-nm emission) at magnification $\times 100$. Before taking the fluorescence images, all the samples were observed using a phase contrast objective of the Nikon Eclipse TS100 to see if there was any tube inside of the Matrigel because this might be undetectable in fluorescence images. The total tube lengths from the fluorescence images were quantified using the AngioQuant v1.33 software (The MathWorks, Natick, MA). The experiments were performed at three independent times.

In Vivo Matrigel Plug Assay

Female athymic nude mice (BALB/c, nu/nu-NCr), 4–6 weeks old, weighing 18–22 g, were purchased from National Cancer Institute–Frederick (Frederick, MD) and treated in accordance with the Johns Hopkins Animal Care and Use Committee procedures. Mice were divided randomly into two groups, but the researchers were not blinded to the groups when performing the experiments. One group of mice ($n = 5$) was injected with the vehicle (5% DMSO in peanut oil), and the other group ($n = 5$) was injected with 60-mg/kg nitroxoline in vehicle, intraperitoneally, once daily. The mice were pretreated for 3 days with DMSO or nitroxoline before a subcutaneous implantation of 0.5 mL of Matrigel containing pro-angiogenic factors—150 ng/mL recombinant mouse vascular endothelial growth factor 164 (VEGF₁₆₄; a soluble mouse VEGF isoform with 164 amino acids) and 200 ng/mL basic fibroblast growth factor (bFGF) (R&D Systems, Minneapolis, MN) at a site near the abdominal midline. Treatment with DMSO or nitroxoline was continued intraperitoneally, once daily, for an additional 7 days. Mice were killed (as described below), and Matrigel plugs were harvested by excision of the plug, fixed with neutral buffered 10% formalin (Sigma-Aldrich), and embedded in paraffin to prepare sections for histochemical staining using Masson trichrome staining, which stains the Matrigel blue and the endothelial cells and vessels red. A cross-section (5 μ m) of the entire Matrigel plug was photographed at magnification $\times 100$ under the Nikon Eclipse TS100 microscope, and erythrocyte-filled blood vessels were counted per field. Five fields in each group were counted, and the mean vessel numbers and their 95% confidence intervals were plotted. The researchers were blinded to the groups during counting the blood vessels on the slides. The experiment was performed once.

Mouse Model for Human Breast Cancer Xenograft

HCC1954 cells (2×10^6) were implanted subcutaneously into female athymic nude mice ($n = 10$) (BALB/c, nu/nu-NCr), 4–6 weeks old, weighing 18–22 g. After tumors became palpable, the

mice were divided into two groups based on the tumor size of each mouse so that the average tumor volume was equal between the two groups. The researchers were not blinded to the groups. One group of mice ($n = 5$) was injected with vehicle (5% DMSO in peanut oil), and the other group ($n = 5$) was injected with 60-mg/kg nitroxoline in vehicle, intraperitoneally, every other day. The tumor volume was measured using a vernier caliper and calculated according to the modified ellipsoid formula:

$$\text{Tumor volume (mm}^3\text{)} = (\text{width})^2 \times (\text{length}) \times \pi / 6.$$

After 30 days of treatment with DMSO or nitroxoline, the mice were killed (as described below), and whole tumor tissues were excised. Each tumor tissue was dissected into two pieces and processed separately for immunohistochemistry and immunoblot analyses.

Mice were given an intraperitoneal injection of 0.5 mL of 250-mg/kg tribromoethanol (Sigma-Aldrich) and were treated with 100% CO₂ when fully anesthetized. Death was verified by an observed lack of breathing, below normal body temperature, and absence of a palpable heartbeat.

Immunohistochemistry and Immunoblot Analysis of Xenograft Breast Tumors

For immunohistochemistry, the HCC1954 xenograft tumor tissues were fixed with a zinc fixative containing 0.1 M Tris-HCl (pH 7.4), 3 mM Ca(C₂H₃O₂)₂, 27 mM Zn(C₂H₃O₂)₂, and 37 mM ZnCl₂ for 2–3 days at room temperature. Then, the fixed tissues were transferred to 0.1 M Tris-HCl (pH 7.4). The tissues were then embedded in paraffin and sliced to obtain 5- μ m sections. The blood vessels in the tumor tissue sections were stained with a mouse anti-human CD31 mAb. To verify the specificity of CD31 staining, sections of vehicle-treated tumors were stained with normal mouse IgG antibody (mock). The slides were then photographed at magnification $\times 100$ using a Nikon Eclipse TS100 microscope. CD31-stained blood vessels were counted per field. Four fields in each group were counted, and the mean vessel numbers and their 95% confidence intervals were plotted using the GraphPad Prism 4.0 software.

For immunoblot analysis, cell lysates were prepared from tumor tissues that were homogenized in ice-cold radioimmunoprecipitation assay buffer (150 mM sodium chloride, 50 mM Tris-HCl, pH 7.5, 1% Nonidet P-40, 0.1% SDS, 2 μ g/mL of aprotinin, 2 μ g/mL of leupeptin, 1 mM PMSF) using a glass Dounce homogenizer (VWR International, West Chester, PA). The lysates were centrifuged at 10 000g at 4°C for 20 minutes to remove tissue and cell debris. The protein concentrations of the lysates were measured using the Bio-Rad Protein Assay kit (Bio-Rad). The lysates containing equal amounts of proteins were boiled for 5 minutes in 2 \times Laemmli buffer, separated on SDS-PAGE, and transferred to nitrocellulose membranes as described earlier. Immunoblot analysis was carried out by incubation with the following primary antibodies—rabbit anti-human acetyl-TP53 (acetyl-K382) (dilution, 1:500), mouse anti-human TP53 (dilution, 1:2000), mouse anti-human TUBA1A (dilution, 1:2000), mouse anti-human RB1 (dilution, 1:1000), mouse anti-human MetAP2 (dilution, 1:2000), and mouse anti-human Met-14-3-3 γ (dilution, 1:1000) at 4°C

overnight, followed by incubation with HRP-conjugated anti-mouse (dilution, 1:2000) or anti-rabbit (dilution, 1:2000) IgG at room temperature for 1 hour. Bound antibodies were detected using ECL as described earlier. The immunoblot signals were quantified using Image J software.

Mouse Model for Orthotopic Bladder Cancer

The orthotopic mouse model used has been described previously (32). Female athymic nude mice ($n = 11$) (Hsd:Athymic Nude-*Foxn1tm*), 8 weeks old, weighing 20–24 g, were purchased from Harlan Laboratories (Indianapolis, IN). Mice were anesthetized with isoflurane. A superficial 6-0 polypropylene purse-string suture was placed around the urethral meatus before a lubricated 24-gauge Jelco angiocatheter (Smiths Medical, St Paul, MN) was passed through the urethra into the bladder. After a single irrigation of the bladder with 100 μ L PBS, KU7-luc cells (2×10^6) were instilled as single-cell suspension in 50 μ L, and the purse-string suture was tied down for a 2.5-hour period, during which the mice were kept anesthetized. Three days after intravesical instillation of KU7-luc cells, orthotopic bladder tumor growth was confirmed via bioluminescence using an IVIS200 Imaging System (Caliper Life Sciences, Hopkinton, MA).

Mice ($n = 11$) were divided into two groups based on the bioluminescence intensity of each tumor so that the average intensity was equal between the two groups. The researchers were not blinded to the groups. The groups were treated with 5% DMSO in saline (vehicle, $n = 5$) or nitroxoline in vehicle (30 mg/kg/day, $n = 6$) by oral administration daily for 2 weeks, starting on day 3. To quantify in vivo tumor burden, animals were imaged on days 7, 11, 16, 21, and 26 in the IVIS200 Imaging System.

At necropsy after 26 days, we analyzed the morphology of the bladders. The whole bladders were removed, fixed in neutral buffered 10% formalin (30 mM NaH_2PO_4 and 40 mM Na_2HPO_4 [pH6.8], and 3.7% formaldehyde), and embedded in paraffin. The paraffin blocks containing whole bladders were used for histology sections. At least one 5- μ m section was obtained from each bladder and stained with hematoxylin and eosin (Sigma-Aldrich) to assess the morphology of bladders. Bladders containing KU7 human cancer cells stain more intensely than normal mouse bladder cells as described previously (32).

For immunoblot analysis, lysates were prepared from mouse bladder tissue using the same method described earlier for xenograft breast tumors. Immunoblot analysis was carried out with the following antibodies: mouse anti-human TP53 (dilution, 1:2000), mouse anti-human Met-14-3-3 γ (dilution, 1:1000), and mouse anti-human RB1 (dilution, 1:1000), followed by HRP-conjugated anti-mouse (dilution, 1:2000) IgG. Bound antibodies were detected using ECL as described earlier. The immunoblot signals were quantified using Image J software and the data from three bladder samples per group were plotted using GraphPad Prism 4.0 software.

Animal procedures were done according to the guidelines of the Canadian Council on Animal Care.

Statistical Analysis

For in vitro experiments, the statistical significance of differences between control and experimental groups were determined by

two-sided Student *t* test, except for the combination index synergy analysis for which one-sample *t* test was used. Results from in vitro experiments were expressed as mean values with 95% confidence intervals from at least three independent experiments. For in vivo studies, the statistical significance of differences between control and experimental groups were determined by two-sided Student *t* test, except for the bioluminescence measurement in the bladder cancer orthotopic xenograft model for which two-way repeated measures ANOVA was used. All statistical tests were two-sided and *P* values less than .05 were considered statistically significant. All statistical analyses were performed using GraphPad Prism 4.0 software.

Results

Screening for Inhibitors of MetAP2 and Endothelial Cell Proliferation and Identification of Nitroxoline as a Promising Hit

Target-Based Screening. To identify novel inhibitors of MetAP2, we performed a high-throughput screen of a library of 175 000 compounds using a contiguous spectrophotometric assay with Met-Pro-pNA as a substrate of MetAP. A total of 294 hits were identified that inhibited MetAP2 activity by at least 50% at 10 μ M concentration. The detailed screening results and hits (data not shown) will be reported elsewhere. Nitroxoline, with its relatively simple chemical structure and good potency (>99% inhibition of MetAP2 activity at 10 μ M concentration), was one of the most potent hits identified in this screen. When the aza-benzenoid core structure of nitroxoline was compared with the spiroepoxide moiety of TNP-470, a well-known inhibitor of MetAP2, we found that the structures were quite distinct (Figure 1, A).

We next evaluated the inhibitory effect of nitroxoline on MetAP2 activity by determining the IC_{50} value. Nitroxoline showed a strong inhibition of MetAP2 enzyme activity ($\text{IC}_{50} = 54.8$ nM, 95% CI = 22.6 to 132.8 nM) (Figure 1, B). In contrast, even the highest concentration (50 μ M) of nitroxoline showed very little inhibition of MetAP1 activity (data not shown). These results demonstrated that nitroxoline had remarkable isoform specificity toward MetAP2.

Cell-Based Screening. In a separate screen, we used the JHDL to identify potential hits that could inhibit endothelial cell proliferation. Although nitroxoline has not been approved in the United States for clinical use, it is used as an antibiotic in several other countries, and therefore, was included in the JHDL. Among the 210 drugs identified that inhibited the proliferation of HUVEC by at least 50%, nitroxoline showed 95.5% inhibition of proliferation at 10 μ M concentration, making it the 97th most potent hit (data not shown). Nitroxoline showed inhibition of HUVEC proliferation with moderate potency ($\text{IC}_{50} = 1.9$ μ M, 95% CI = 1.54 to 2.39 μ M) (Figure 1, C).

Mechanism of Inhibition by Nitroxoline. The ability of nitroxoline to inhibit both MetAP2 activity and endothelial cell proliferation suggested that MetAP2 inhibition, at least in part, could be the mechanism responsible for inhibition of endothelial cell proliferation. Therefore, we determined whether nitroxoline inhibited MetAP2 activity in endothelial cells. One of the well-established

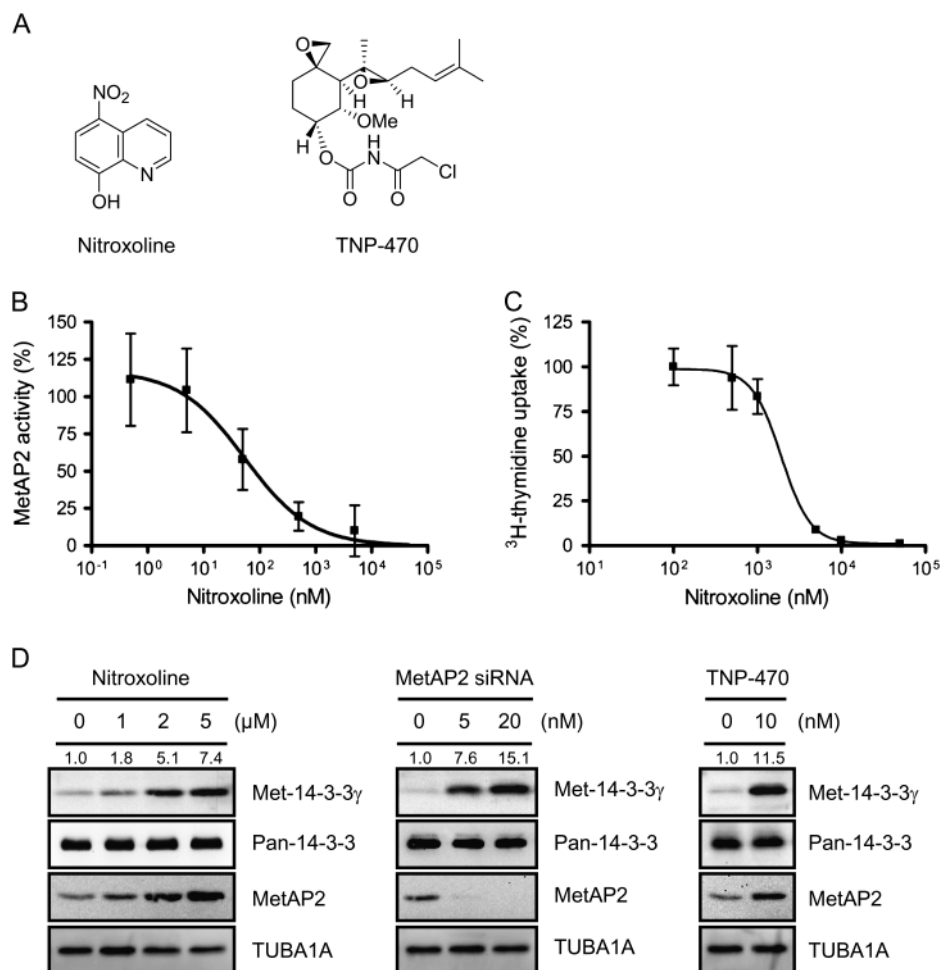


Figure 1. Effect of nitroxoline on type 2 methionine aminopeptidase (MetAP2) activity and human umbilical vein endothelial cells (HUVEC) proliferation. **A**) Chemical structures of nitroxoline and TNP-470. The aza-benzenoid core structure of nitroxoline is structurally distinct from the spiroepoxide-containing TNP-470. **B**) Analysis of dose–response effect of nitroxoline (0.5 nM–50 μ M) on the activity of MetAP2. Purified recombinant MetAP2 was incubated with varying concentration of nitroxoline for 30 minutes at room temperature and analyzed for the enzyme activity. Nitroxoline, at the lowest concentration (0.5 nM), showed an approximately 10% increase in MetAP2 activity; therefore, more than 100% activity is shown on the y-axis. Mean percentages of substrate cleavage by MetAP2 from four independent experiments are shown. **Error bars** = 95% confidence intervals. **C**) Analysis of dose–response effect of nitroxoline (0.1–50 μ M) on HUVEC proliferation. Cells

were treated with varying concentration of nitroxoline for 24 hours and the mean percentages of ³H-thymidine uptake from four independent experiments are shown. **Error bars** = 95% confidence intervals. **D**) Analysis of N-terminal methionine processing of 14-3-3 γ protein. HUVEC were treated with 1, 2, or 5 μ M nitroxoline (far left panel) or 10-nM TNP-470 (far right panel) for 24 hours. In a separate experiment, HUVEC were transfected with control or MetAP2 small-interfering RNAs (center panel) for 24 hours. Cell lysates were analyzed for the levels of methionine on 14-3-3 γ (Met-14-3-3 γ), 14-3-3, MetAP2, and tubulin, alpha 1a (TUBA1A) proteins by immunoblotting. Met-14-3-3 γ protein levels were normalized to the level of 14-3-3 protein for each concentration, and their relative differences with the control are shown. In each panel, representative blots from three independent experiments are shown.

substrates for both MetAP2 and MetAP1 is 14-3-3 γ (43). Inhibition of either of the endogenous MetAPs leads to the retention of the N-terminal initiator methionine on 14-3-3 γ (Met-14-3-3 γ), which can be detected in an immunoblot analysis. Treatment of HUVEC with nitroxoline led to a dose-dependent increase in the level of Met-14-3-3 γ protein, whereas the total 14-3-3 protein level remained unchanged (Figure 1, D, left panel). The use of siRNAs against MetAP2 (Figure 1, D, center panel) or TNP-470 (Figure 1, D, right panel) in HUVEC caused a great increase in the level of Met-14-3-3 γ protein, further confirming that nitroxoline could inhibit MetAP2 in the cells. Similar to TNP-470, nitroxoline also showed an increase in the level of MetAP2 protein itself (Figure 1, D, left and right panels).

Effect of Nitroxoline and TNP-470 on MetAP2 Function and HUVEC Senescence

Effect of Nitroxoline and TNP-470 on Proteins That May Have a Role in MetAP2 Inhibition. We and others have previously shown that the antiproliferative effect of TNP-470 on HUVEC was mediated through the activation of TP53, which increased the expression of p21 protein. An increase in the level of p21 protein subsequently inhibited the CCNE1–CDK2 complex, which in turn inhibited RB1 phosphorylation (16,17). Therefore, we compared the effects of nitroxoline on the expression of these proteins with that of TNP-470 to assess the involvement in MetAP2 inhibition. Similar to TNP-470, HUVEC treated with nitroxoline showed an increase in the level of TP53 protein (Figure 2, A). Both

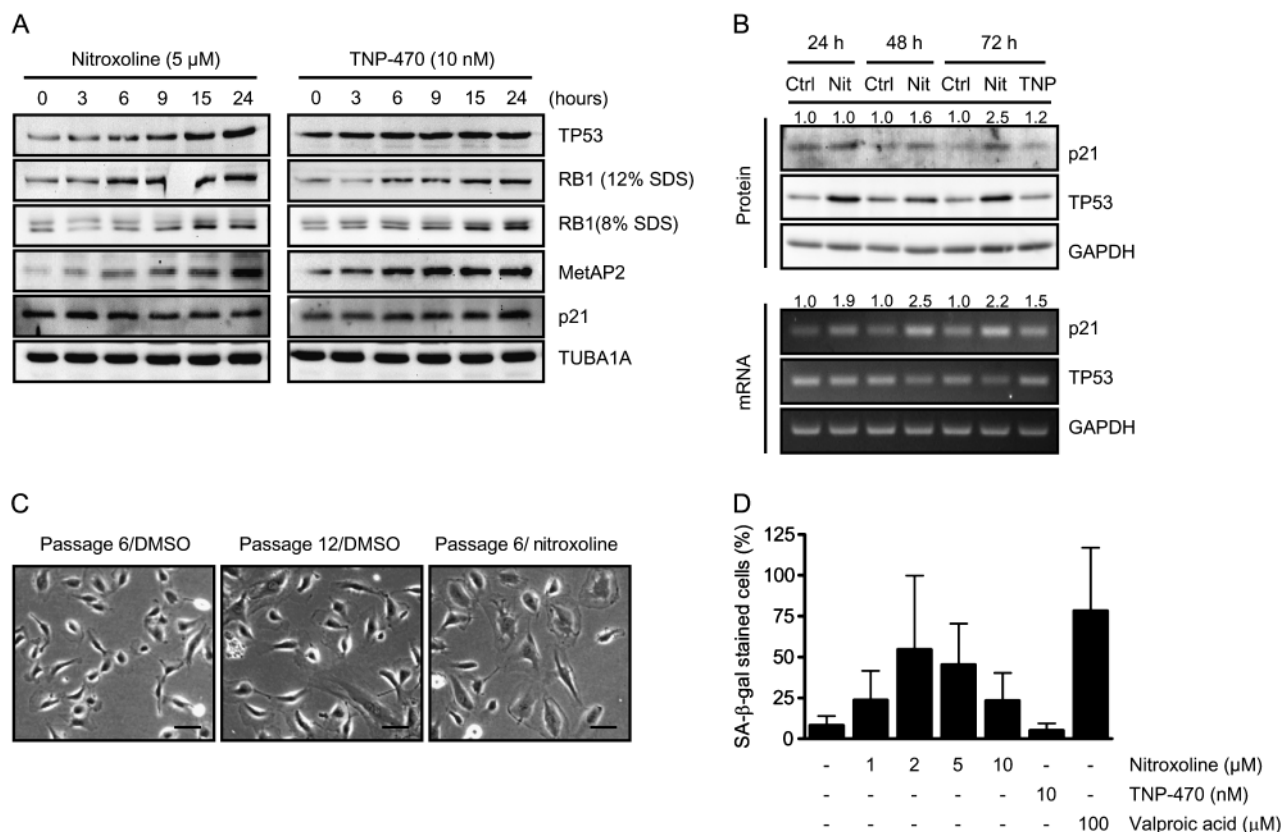


Figure 2. Comparing the effects of nitroxoline and TNP-470 on tumor protein p53 (TP53) pathway and premature senescence in human umbilical vein endothelial cells (HUVEC). **A**) Immunoblot analysis of proteins belong to TP53 pathway and type 2 methionine aminopeptidase (MetAP2) protein level. Cells were treated with either nitroxoline (5 μM) or TNP-470 (10 nM) for indicated the time periods and cell lysates were analyzed for TP53, retinoblastoma 1 (RB1) (12% sodium dodecyl sulfate [SDS] and 8% SDS), MetAP2, p21, and tubulin, alpha 1a (TUBA1A) by immunoblotting. **B**) Analysis of protein and mRNA levels of TP53 and p21. Cells were treated with either vehicle control (Ctrl), 5 μM nitroxoline (Nit) or 10-nM TNP-470 (TNP) for the indicated time periods. Cells lysates were analyzed for TP53 and p21 levels by either immunoblot or reverse transcriptase–polymerase chain reaction. Glyceraldehyde 3-phosphate dehydrogenase (GAPDH) was used as the loading control. The p21 protein and mRNA levels were normalized to

the levels of GAPDH protein and mRNA, respectively, for each time point and their relative differences with the corresponding controls are shown. For both A) and B), representative blots from three independent experiments are shown. **C**) Analysis of cell morphology. After passage 6 or passage 12, cells were treated with either dimethyl sulfoxide (DMSO) or nitroxoline (5 μM) for 24 hours and images were taken at $\times 200$ magnification. **Scale bar** = 50 μm. **D**) Analysis of premature senescence. Cells were treated with varying concentration of nitroxoline (1, 2, 5, and 10 μM), TNP-470 (10 nM) or valproic acid (100 μM) for 72 hours, and the induction of premature senescence was monitored by detecting the level of senescence-associated β -galactosidase (SA- β -gal) activity. SA- β -gal-stained cells and total cells were counted, and mean percentages of SA- β -gal-stained cells vs total cells from three independent experiments are shown. **Error bars** = 95% confidence intervals.

nitroxoline and TNP-470 also caused an increase in the total amount of RB1 protein (observed on 12% of SDS-PAGE). A lower percent (such as 8%) of SDS-PAGE allows separation of the different phosphorylated forms of RB1; the lowest band representing the hypophosphorylated form (17). We noted that both nitroxoline and TNP-470 increased the level of hypophosphorylated RB1 protein with increased incubation time (Figure 2, A). Both nitroxoline and TNP-470 also caused an increase in the level of MetAP2 protein. However, unlike TNP-470, nitroxoline showed no effect on the level of p21 protein after 24 hours of treatment (Figure 2, A). Cells treated with nitroxoline for a longer period (for up to 72 hours) showed sustained increase in the level of TP53 protein level, whereas in cells treated with TNP-470 for the same period of time, the level of TP53 protein returned to that of the untreated control (Figure 2, B). However, treatment with nitroxoline showed a decrease in the TP53 mRNA level in a time-dependent manner. The level of p21 protein and mRNA increased

when cells were treated with nitroxoline for up to 72 hours (Figure 2, B).

Effect of Nitroxoline and TNP-470 on HUVEC Morphology and Senescence. Next, we wanted to compare the effects of nitroxoline and TNP-470 on HUVEC morphology and senescence. When HUVEC were treated with nitroxoline, we consistently observed an increase in cell size and morphological changes similar to the changes after extended passages in cell culture (Figure 2, C). In contrast we did not observe any remarkable change in HUVEC morphology with TNP-470 (data not shown).

It is known that primary endothelial cells become senescent after repeated passages in culture, a process referred to as replicative senescence [reviewed in (44)]. Senescence can also be induced in response to acute stress that involves TP53 activation, which is referred to as stress-induced premature senescence (45). We investigated whether the morphological changes observed in HUVEC

treated with nitroxoline was accompanied by premature senescence. Nitroxoline induced premature senescence in HUVEC in a biphasic manner and peaked at the 2–4 μM concentration range (Figure 2, D). In contrast, TNP-470 did not induce premature senescence, either at 10 nM concentration (Figure 2, D), which is 20 times higher than the IC_{50} value of TNP-470 for HUVEC proliferation, or at even lower concentrations (0.1–5 nM) (data not shown). Representative images of induction of senescence in HUVEC by nitroxoline, TNP-470, and valproic acid are shown in Supplementary Figure 1, A and B (available online).

Effect of Nitroxoline on TP53 Acetylation and Sirtuin Activities

The aza-benzenoid core structure of nitroxoline is similar to some well-known sirtuin inhibitors (AGK2, EX527) and activators such as SRT1720 [reviewed in (46)]. We conducted the PubChem similarity search for the aza-benzenoid moieties in nitroxoline and sirtuin modulators using the Tanimoto index, a similarity measurement tool for chemical structures (perfect match, Tanimoto index = 1; no match, Tanimoto index = 0) (47). The quinoline fragment of AGK2 (Supplementary Figure 2, available online) and the aza-benzenoid moieties of the aforementioned sirtuin modulators revealed a high degree of similarities (Tanimoto indices = 0.69 to 0.78) (Supplementary Figure 2, available online).

The structural similarities of nitroxoline and sirtuin modulators prompted us to determine the effect of nitroxoline on sirtuin activities. Of the seven isoforms of human sirtuins, SIRT1 has been shown to deacetylate TP53 specifically at lysine 382 (K382) (23). In contrast, SIRT2 has been reported to deacetylate TUBA1A as well as histone H3 at K9 (48). Both SIRT2 and SIRT3 are known to deacetylate histone H4 at the K16 position (49). Therefore, we performed an immunoblot analysis to assess the effect of nitroxoline on the level of acetylated sirtuin substrates in HUVEC. There was no effect of nitroxoline on the level of acetylated TUBA1A or histone H3, whereas sirtinol (plant SIR2 inhibitor), and particularly the HDAC inhibitor TSA, induced an increase in the levels of acetylated TUBA1A and histone H3 (Figure 3, A). We noted a 3.8-fold increase in the level of acetylated TP53 (acetyl-K382) after treating HUVEC with 5 μM nitroxoline for 20 hours; there was no change in the level of acetylated TP53 (acetyl-K382) with a high concentration of nitroxoline (20 μM), or a shorter incubation period (6 hours). In contrast, when HUVEC were treated with TSA, an increase in the level of acetylated TP53 (acetyl-K382) was observed at an earlier time point, which returned to that of the control level after 20 hours of treatment.

We further analyzed if the effect of nitroxoline on the level of acetylated TP53 (acetyl-K382) was dose responsive by treating HUVEC with varying concentrations of nitroxoline for 20 hours. A biphasic induction of an increased level of acetylated TP53 (acetyl-K382) was noted with a peak induction at 4–5 μM of nitroxoline; a pattern that was similar to the changes in the level of TP53 protein (Figure 3, B). We also determined the effect of varying concentrations of nitroxoline on the levels of acetylated TUBA1A and histone H3 to see if any concentration range of nitroxoline could affect the acetylation status of the proteins and observed that there was no effect (Figure 3, B). Similarly, there was no obvious change in SIRT1 protein level by nitroxoline.

Because nitroxoline caused an increase in the level of acetylated TP53 (acetyl-K382), we investigated whether nitroxoline also affected the activity of sirtuin enzymes (23). We developed an *in vitro* assay based on deacetylation of acetylated TP53 (acetyl-K382) peptides by SIRT1 or deacetylation of acetylated histone H4 (acetyl-K16) peptides by SIRT2 and SIRT3. The level of the remaining acetylated peptides was detected in a dot blot assay using the rabbit anti-human acetyl-TP53 (acetyl-K382) or rabbit anti-human acetyl-histone H4 (acetyl-K16) antibody (Supplementary Figure 3, available online). A dose-dependent inhibition of SIRT1 activity (IC_{50} = 20.2 μM , 95% CI = 8.3 to 49.3 μM) was observed when the recombinant SIRT1 protein was treated with nitroxoline (0.5–50 μM concentration) (Figure 3, C and D). A dose-dependent inhibition of SIRT2 activity (IC_{50} = 15.5 μM , 95% CI = 4.9 to 49.0 μM) was observed when recombinant SIRT2 was treated with nitroxoline (1–50 μM concentration), whereas there was no effect on the activity of SIRT3 (Figure 3, E and F). These results demonstrated that nitroxoline inhibited both SIRT1 and SIRT2 activities *in vitro*, but with slightly higher potency against SIRT2 activity.

Effect of Concurrent Inhibition of SIRT1 and MetAP2 Activities on the Level of Acetylated TP53

Though SIRT2 is known to deacetylate TUBA1A protein, the pharmacological inhibition of SIRT2 activity is not sufficient to induce TUBA1A acetylation in mammalian cells (50). However, in the presence TSA, a SIRT2 inhibitor is known to substantially enhance the acetylation of TUBA1A protein in cells (50,51). This is presumably because of a cooperative action of HDAC6 and SIRT2 on the deacetylation of TUBA1A (48). To determine whether there was an effect of nitroxoline on the level of acetylated TUBA1A protein or histone H3 protein in the presence of TSA, we treated HUVEC with both low and high concentrations of nitroxoline for 24 hours, and the levels of several acetylated sirtuin substrates were determined. As shown in Figure 4, A, nitroxoline alone did not show an increase in the level of acetylated TUBA1A protein or acetylated histone H3 protein in HUVEC, even though it increased the level of acetylated TP53 (acetyl-K382) protein. However, in the presence of TSA, nitroxoline (15 μM) substantially increased the level of both acetylated TUBA1A and acetylated histone H3 (Figure 4, A). The results indicated that nitroxoline inhibited SIRT2 activity in HUVEC at a concentration similar to its IC_{50} value for inhibition of SIRT2 activity *in vitro* (Figure 3, E and F). When we treated HUVEC with EX527 (5 and 15 μM), a specific inhibitor of SIRT1, an increase in the level of acetylated TP53 (acetyl-K382) protein was observed (Figure 4, B). However, in the presence of TSA, there was little change in the level of acetylated TP53 (acetyl-K382) protein or in acetylated TUBA1A and histone H3 proteins. These results suggested that the increase in the level of acetylated TUBA1A protein by nitroxoline was attributable to the inhibition of SIRT2 activity.

Although nitroxoline inhibited SIRT2 activity with slightly higher potency than SIRT1 (IC_{50} = 15.5 μM for SIRT2 vs IC_{50} = 20.2 μM for SIRT1) (Figure 3, C and F), it inhibited SIRT1 activity with slightly higher potency than SIRT2 when we assessed the inhibition of enzyme activities in cell culture based on the level of

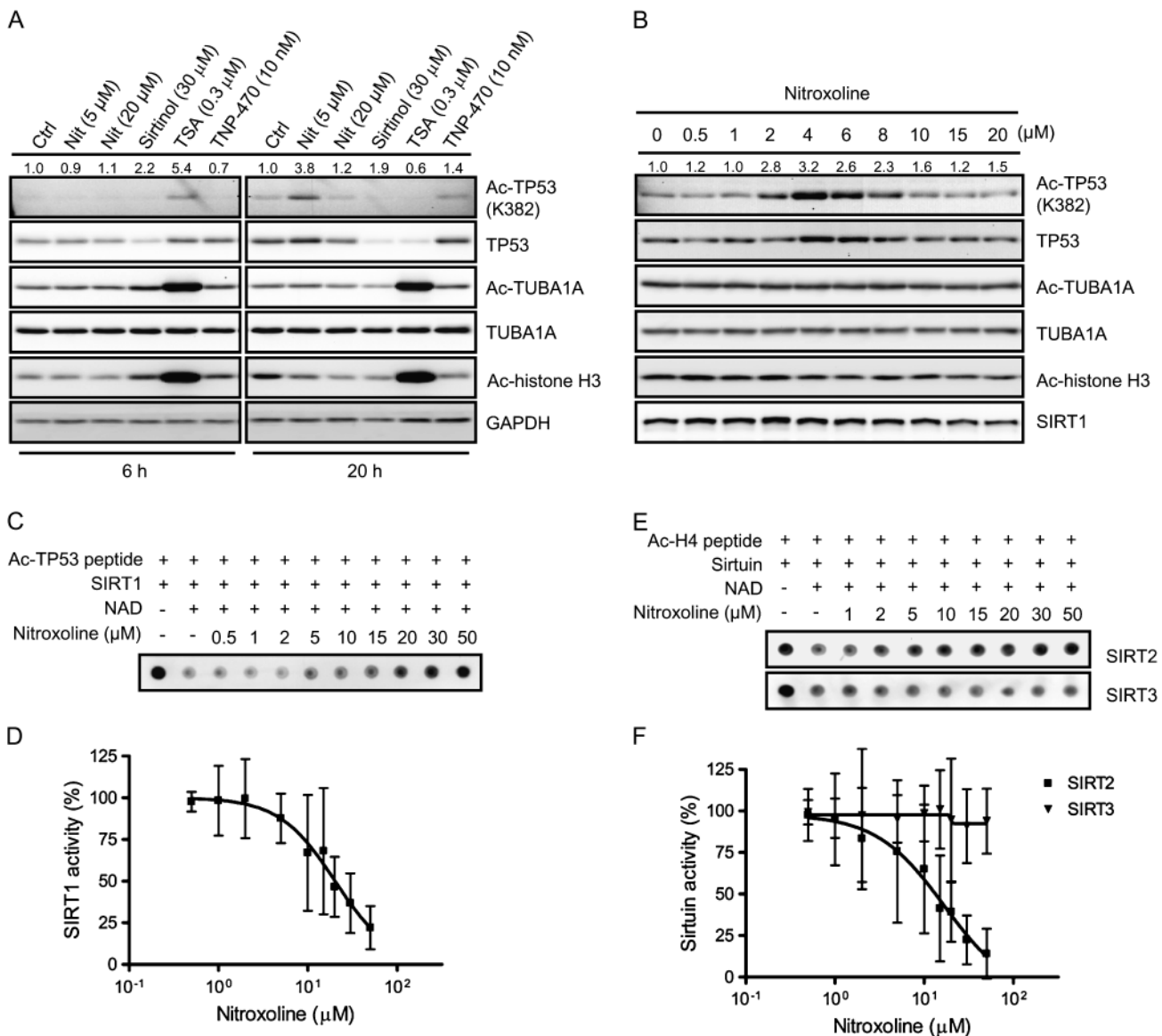


Figure 3. Effect of nitroxoline on sirtuin activities in human umbilical vein endothelial cells (HUVEC). **A** Immunoblot analysis to detect sirtuin activity. Cells were treated with vehicle control (Ctrl), nitroxoline (Nit; 5 μM or 20 μM), sirtinol (30 μM), trichostatin A (TSA; 0.3 μM) and TNP-470 (10 nM) for either 6 or 20 hours, and cell lysates were analyzed for the following total and acetylated proteins—TP53 (acetyl-K382), tubulin, alpha 1a (TUBA1A), and histone H3 proteins by immunoblotting. Glyceraldehyde 3-phosphate dehydrogenase (GAPDH) was used as the loading control. **B** Dose-response effect of nitroxoline on the level of Ac-TP53. Cells were treated with varying concentrations of nitroxoline for 20 hours and lysates were analyzed for the following total and acetylated proteins—TP53 (acetyl-K382), TUBA1A, and histone H3 by immunoblotting. TUBA1A was used as the loading control. In both (A) and (B), Ac-TP53 protein levels were normalized to total TP53 protein levels, and their relative differences with the corresponding controls are shown. The blots are representative of three independent experiments. **C** Dot blot analysis of *in vitro* enzyme

activity of SIRT1. Recombinant human SIRT1 was treated with increasing concentrations (0.5–50 μM) of nitroxoline for 2 hours and *in vitro* enzyme assay was conducted using acetylated TP53 (acetyl-K382) peptide (Ac-TP53 peptide) in the presence or absence of nicotinamide adenine dinucleotide (NAD), a cofactor of SIRT1. **D** Quantitative analysis of SIRT1 activity. Intensity of each dot was quantified using ImageJ software. Mean percentages of the acetylation level of TP53 peptide substrate from three independent experiments are shown. **Error bars** = 95% confidence intervals. **E** Analysis of *in vitro* enzyme activities of SIRT2 and SIRT3. Similar to (C), recombinant human SIRT2 and SIRT3 were treated with increasing concentrations (1–50 μM) of nitroxoline and acetylated histone H4 (acetyl-K16) peptide (Ac-H4 peptide) was used as the substrate. **F** Quantitative analysis of SIRT2 and SIRT3 activities. Intensity of each dot was quantified using ImageJ software. Mean percentages of the acetylation level of histone H4 peptide substrate from three independent experiments are shown. **Error bars** = 95% confidence intervals. Ac = acetylated.

endogenous substrates of respective enzymes. To determine whether this discrepancy between *in vitro* and cell culture activities was because of concurrent inhibition of SIRT1 and MetAP2 activities by nitroxoline, we used specific siRNAs and small-molecule inhibitors to inhibit the expression and activity, respectively, of

SIRT1 and MetAP2 proteins, and examined the effect of their simultaneous inhibition on the level of acetylated TP53 (acetyl-K382) protein in HUVEC. MetAP2 siRNA substantially reduced the expression of MetAP2 protein, as verified by an immunoblot analysis (Figure 4, C). Next, we tested two SIRT1 siRNAs

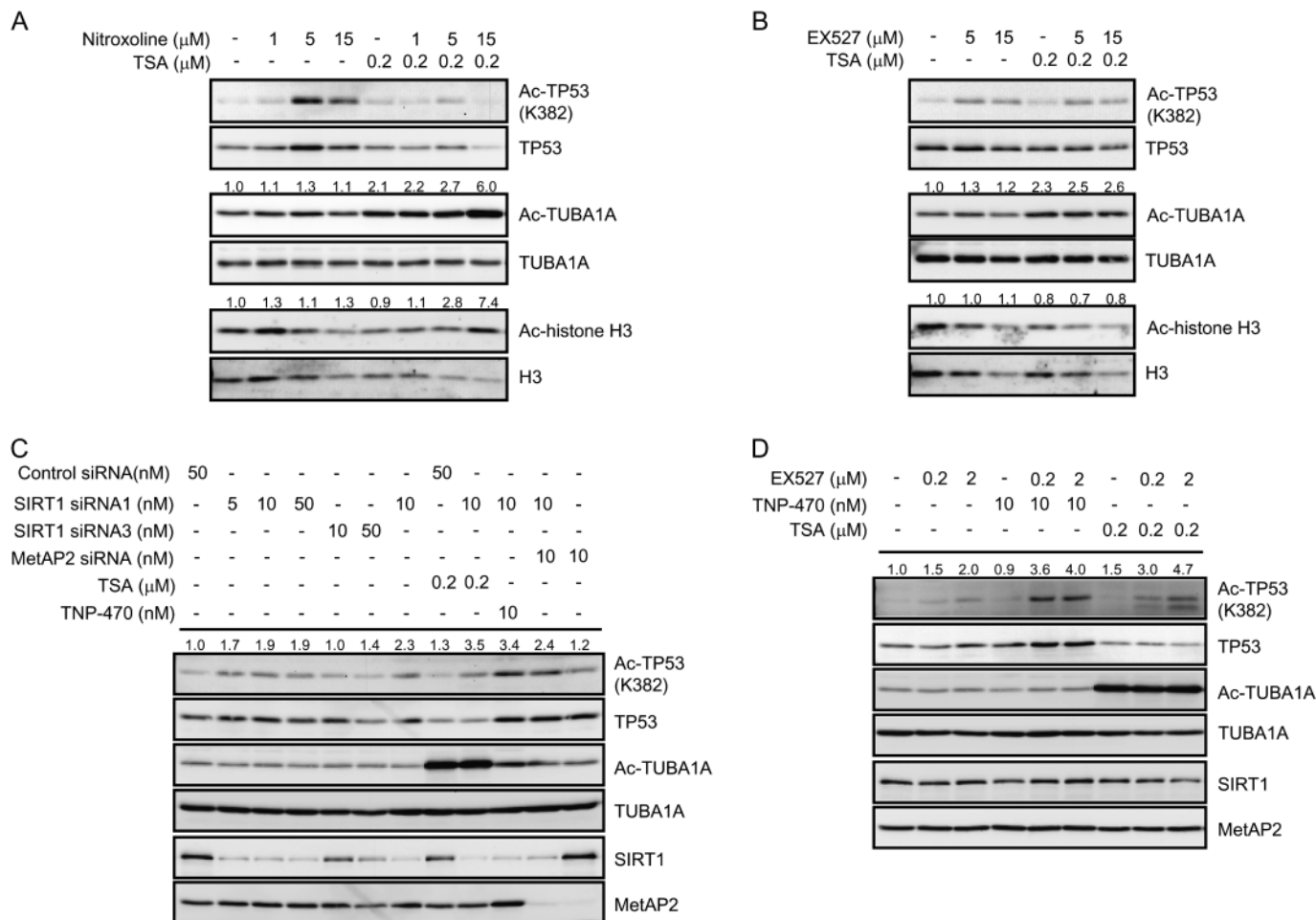


Figure 4. Effect of concurrent inhibition of SIRT1 and type 2 methionine aminopeptidase (MetAP2) on acetylated TP53 in human umbilical vein endothelial cells (HUVEC). **A** Effect of nitroxoline on the acetylation status of various sirtuin substrates. Cells were treated with 1, 5, or 15 μM nitroxoline in the presence or absence of 0.2 μM trichostatin A (TSA) for 24 hours and lysates were analyzed by immunoblotting for the following total and acetylated proteins—TP53 (acetyl-K382), tubulin, alpha 1a (TUBA1A), and histone H3. **B** Effect of EX527, a SIRT1 inhibitor, on the acetylation status of various sirtuin substrates in the presence or absence of TSA. Cells were treated with 0, 5, or 15 μM EX527 with or without TSA (0.2 μM) for 24 hours and lysates were analyzed by immunoblotting. In both (A) and (B), the acetylated TUBA1A and histone H3 levels were normalized to their respective total protein levels and the relative differences with the corresponding controls are shown. **C** Effect of small-interfering RNAs (siRNAs) against SIRT1 and MetAP2

on acetylated TP53 (acetyl-K382). Cells were transfected with control siRNA, two different SIRT1 siRNAs (siRNA1 and siRNA3) or MetAP2 siRNA for 24 hours and treated with either TSA (0.2 μM) or a MetAP2 inhibitor, TNP-470 (10 nM), for an additional 24 hours. Cells lysates were analyzed for Ac-TP53 (acetyl-K382), acetylated TUBA1A, SIRT1 and MetAP2 proteins by immunoblotting. **D** Effect of SIRT1 and MetAP2 inhibitors on the level of acetylated TP53 (acetyl-K382). Cells were treated with 0, 0.2, and 2 μM EX527 in the presence or absence of TNP-470 (10 nM) or TSA (0.2 μM), for 24 hours. Cell lysates were analyzed for acetylated TP53 (acetyl-K382), acetylated TUBA1A, SIRT1, and MetAP2 by immunoblotting. In both (C) and (D), Ac-TP53 protein levels were normalized to total TP53 protein levels and their relative differences with the corresponding controls are shown. The blots in all panels are representative of three independent experiments. Ac = acetylated.

(siRNA1 and siRNA3) that have two different target sites in SIRT1 mRNA. Although neither SIRT1 siRNAs could completely knockdown the expression of SIRT1 protein, SIRT1 siRNA1 was more efficient than SIRT1 siRNA3 in reducing the SIRT1 protein level in HUVEC (Figure 4, C). Thus, subsequent experiments were done with SIRT1 siRNA1. Compared with control siRNA, SIRT1 siRNA1 caused a slight increase in the level of acetylated TP53 (acetyl-K382) protein; the level was further increased in the presence of either TNP-470 or MetAP2-siRNA (Figure 4, C). Substantial increase in the level of acetylated TP53 (acetyl-K382) protein was noted upon TSA treatment when SIRT1 siRNA was used.

In a complementary approach, we tested the effect of EX527, an SIRT1-specific inhibitor, and TNP-470, an MetAP-2-specific inhib-

itor on the level of acetylated TP53 (acetyl-K382). A slight increase in the level of acetylated TP53 (acetyl-K382) protein was noted with EX527 alone, and an up to fourfold increase was noted when HUVEC were treated with both EX527 and TNP-470 (Figure 4, D). Consistent with siRNA experiments, treatment of HUVEC with TSA in combination with low concentrations of EX527 (0.2 and 2 μM) also showed substantial increase in the level of acetylated TP53 (acetyl-K382).

Analysis of Potential Synergy Between SIRT1 and MetAP2 Inhibitors

Next, we determined if there was synergy between the inhibitors of SIRT1 and MetAP2 in inhibiting endothelial cell proliferation. HUVEC were treated with various concentrations of EX527 in the

presence or absence of TNP-470, and the levels of acetylated TP53 (acetyl-K382) protein were detected by immunoblot analysis. We noted that EX527 alone caused up to 2.5-fold increase in the level of acetylated TP53 (acetyl-K382) protein, and up to 4.7-fold increase was noted when a combination of EX527 and TNP-470 was used (Figure 5, A). Similar to nitroxoline, the induction of an increased level of acetylated TP53 (acetyl-K382) by EX527 alone or EX527 and TNP-470 combination showed a biphasic pattern, although the increased level of acetylation was seen with wider range of EX527 concentrations than nitroxoline. To determine the optimal concentrations of EX527 and TNP-470 suitable for detection of potential synergy, we obtained the IC_{50} values of both compounds for inhibition of HUVEC proliferation. EX527 showed a much weaker inhibition of cell proliferation (IC_{50} = 9.1 μ M, 95% CI = 8.0 to 10.2 μ M) than TNP-470 (IC_{50} = 0.56 nM, 95% CI = 0.35 to 0.90 nM) (Figure 5, B). We then analyzed whether the combined effect of the two compounds was synergistic by using the Chou-Talalay algorithm for analysis of combination index (41). We chose four combinations of the two drugs with a fixed concentration ratio as follows—combination of 1 IC_{50} , 9.1 μ M EX527 + 0.56 nM TNP-470; combination of 1/2 IC_{50} , 4.55 μ M

EX527 + 0.28 nM TNP-470; combination of 1/4 IC_{50} , 2.27 μ M EX527 + 0.14 nM TNP-470; and combination of 1/8 IC_{50} , 1.13 μ M EX527 + 0.07 nM TNP-470. A combination of EX527 and TNP-470 showed a strong synergy in inhibition of HUVEC proliferation for all four combinations of varying inhibitor concentrations tested; combination of 1/8 of IC_{50} , mean combination index = 0.557, 95% CI = 0.139 to 0.975, P = .045; combination of 1/4 of IC_{50} , mean combination index = 0.391, 95% CI = 0.106 to 0.675, P = .0116; combination of 1/2 of IC_{50} , mean combination index = 0.352, 95% CI = 0.147 to 0.558, P = .005; combination of 1 IC_{50} , mean combination index = 0.244, 95% CI = 0.093 to 0.396, P = .002 (Figure 5, C).

Inhibition of SIRT1 using pharmacological or genetic methods is known to induce a premature senescence-like phenotype in HUVEC and other mammalian cells (24,26). Consistent with our previously presented data, nitroxoline induced senescence in HUVEC at 5 μ M concentration (control vs nitroxoline, mean = 8.67 vs 45.33%, difference = 36.66%, 95% CI = 12.53 to 78.13, P = .010), whereas TNP-470 had no effect at 10 nM concentration (Figure 5, D) that was 20 times greater than the concentration that induced 50% inhibition of HUVEC proliferation. In agreement

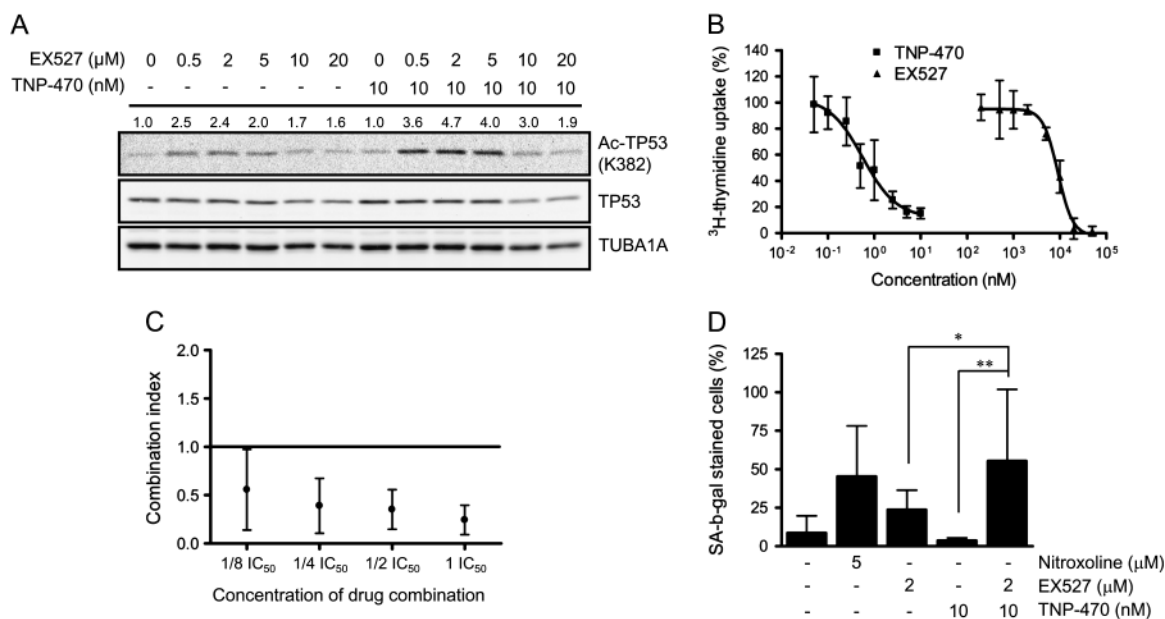


Figure 5. Effect of concurrent inhibition of type 2 methionine aminopeptidase (MetAP2) and SIRT1 on human umbilical vein endothelial cells (HUVEC) proliferation and senescence. **A)** Immunoblot analysis of the level of acetylated TP53 (acetyl-K382) after inhibition of MetAP2 and SIRT1 activities. Cells were treated with varying concentrations of EX527 (0.5–20 μ M) with or without 10 nM TNP-470 for 24 hours, and lysates were analyzed by immunoblotting for Ac-TP53, TP53, and tubulin, alpha 1a (TUBA1A). TUBA1A was the loading control. Ac-TP53 protein levels were normalized to total TP53 protein levels and their relative differences with the corresponding controls are shown. The blots are representative of three independent experiments. Ac = acetylated. **B)** Determination of half maximal inhibitory concentration (IC_{50}) values of TNP-470 and EX527 for cell proliferation experiment. Mean percentages of 3 H-thymidine uptake by the cells from three independent experiments are shown. **Error bars** = 95% confidence intervals. **C)** Analysis of synergism between TNP-470 and EX527 on cell proliferation. The IC_{50} values obtained in (B) were used. Cells were treated with different concentration of TNP-470 or EX527 alone or a

combination of both drugs with fixed ratio (combination of 1 IC_{50} , 9.1 μ M EX527 + 0.56 nM TNP-470; combination of 1/2 IC_{50} , 4.55 μ M EX527 + 0.28 nM TNP-470; combination of 1/4 IC_{50} , 2.27 μ M EX527 + 0.14 nM TNP-470; and combination of 1/8 IC_{50} , 1.13 μ M EX527 + 0.07 nM TNP-470) for 24 hours, and 3 H-thymidine incorporation was measured. The combination index values for the drug combination are shown on the y-axis. Four different combinations of EX527 and TNP-470 are shown on the x-axis. Mean combination index from three independent experiments are shown. **Error bars** = 95% confidence intervals. **D)** Effects of nitroxoline (5 μ M), EX527 (2 μ M), and TNP-470 (10 nM) on senescence. Cells were treated with single drugs or a combination of EX527 and TNP-470 for 5 days and stained with senescence-associated β -galactosidase (SA- β -gal). Mean percentages of SA- β -gal-stained cells vs total cells from three independent experiments are shown. **Error bars** = 95% confidence intervals. EX527 vs EX527 and TNP-470 combination, * P = .048; TNP-470 vs EX527 and TNP-470 combination, ** P = .009. All P values were calculated using the two-sided Student t test.

with a previous report (26), EX527 at 2 μM was sufficient to induce premature senescence in HUVEC (control vs EX527, mean = 8.67 vs 23.67%, difference = 15%, 95% CI = 10.92 to 36.41, $P = .019$) (Figure 5, D). A strong induction of premature senescence was observed when HUVEC were treated with a combination of EX527 and TNP-470 (for control vs EX527 and TNP-470 combination, mean = 8.67% vs 55.33%, difference = 46.66%, 95% CI = 15.75 to 77.59, $P = .014$; for EX527 vs EX527 and TNP-470 combination, mean = 23.67% vs 55.33%, difference = 31.66%, 95% CI = 0.48 to 62.85, $P = .048$; and for TNP-470 vs EX527 and TNP-470 combination, mean = 3.73% vs 55.33%, difference = 51.60%, 95% CI = 21.49 to 81.71, $P = .009$). No senescence was observed with TNP-470 alone.

Effect of Nitroxoline on Angiogenesis In Vitro and In Vivo

To determine whether nitroxoline had any effect on angiogenesis in vitro, we assessed the formation of endothelial tubes in a three-dimensional assay. The HUVEC tube formation was inhibited by nitroxoline in a dose-dependent manner (Figure 6, A, top panel). Previously, it has been shown that SIRT1 inhibition was sufficient to inhibit angiogenesis both in vitro and in vivo (52). Inhibition of endothelial tube formation was noted with 1 μM EX527; however, there was no inhibition of tube formation with 10 nM TNP-470 (Figure 6, A, bottom panel), a concentration sufficient to inhibit HUVEC proliferation in cell culture. A strong inhibition of tube formation was noted when HUVEC were treated with a combination

of EX527 and TNP-470 (Figure 6, A, bottom panel). The quantitative data on tube lengths are shown in Figure 6, B. The combination of EX527 and TNP-470 synergistically inhibited the tube formation (for control vs EX527 and TNP-470 combination, mean length = 15 110 vs 2284 [arbitrary unit], difference = 12826, 95% CI = 10780 to 14870, $P < .0001$; for EX527 vs EX527 and TNP-470 combination, mean length = 8680 vs 2284 [arbitrary unit], difference = 6396, 95% CI = 4355 to 8438, $P = .0010$; and for TNP-470 vs EX527 and TNP-470 combination, mean length = 13630 vs 2284 [arbitrary unit], difference = 11 346, 95% CI = 7489 to 15 200, $P = .0012$).

To determine whether nitroxoline had an effect on angiogenesis in vivo, we performed a Matrigel plug assay in 10 female athymic nude mice (BALB/c, nu/nu-NCr). Mice were injected with either vehicle ($n = 5$) or nitroxoline ($n = 5$) intraperitoneally, once daily for 3 days, and Matrigel plugs containing VEGF and bFGF were injected subcutaneously into mice. Treatment with DMSO or nitroxoline was continued, once daily, for an additional 7 days. Ten days after initial treatment, the Matrigel plugs were removed and photographed (Figure 6, C), and the newly invaded blood vessels were assessed microscopically (Figure 6, D). Compared with vehicle, nitroxoline at 60 mg/kg reduced the number of new microvessels by 63% (vehicle vs nitroxoline, mean = 48.6 vs 20 microvessels, difference = 28.6 microvessels, 95% CI = 13.49 to 43.71 microvessels, $P = .002$) (Figure 6, D and E).

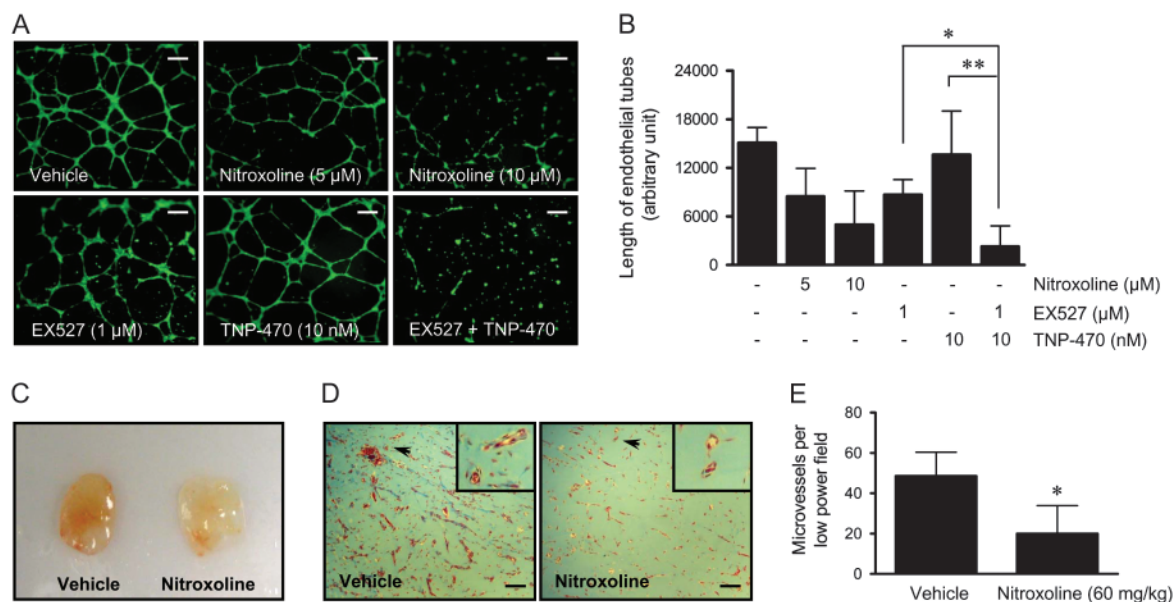


Figure 6. Effect of nitroxoline on angiogenesis in vitro and in vivo. **A**) Effect of nitroxoline or SIRT1 and type 2 methionine aminopeptidase (MetAP2) inhibitors on endothelial tube formation. Human umbilical vein endothelial cells (HUVEC) were placed on Matrigel in the presence or absence of each drug and incubated for 24 hours. The cells were stained with Calcein-AM and tubes were observed under a fluorescence microscope at $\times 100$ magnification. Representative images are shown. **Scale bar** = 200 μm . **B**) Quantitative analysis of mean tube lengths from three independent experiments are shown. **Error bars** = 95% confidence intervals. EX527 vs EX527 and TNP-470 combination, $*P = .001$; TNP-470 vs EX527 and TNP-470 combination, $**P = .0012$. All P values were calculated using the two-sided Student t test. **C**) Analysis of in vivo angiogenesis

using Matrigel plug assay. Ten female athymic nude mice (BALB/c, nu/nu-NCr) were injected with vehicle or 60-mg/kg nitroxoline intraperitoneally (five mice per group) and Matrigel plug assay was performed. Representative Matrigel plugs (five mice per group) are shown. **D**) Representative images of Masson trichrome staining of Matrigel plugs. **Arrowheads** indicate erythrocyte-filled microvessels (insets show the magnified view). Magnification $\times 100$. **Scale bar** = 150 μm . **E**) Quantitative analysis of microvessels in the Matrigel plugs shown in (D) by counting five randomly selected fields in low-power (magnification $\times 100$) fields. Mean number of microvessels in vehicle-treated and nitroxoline-treated groups are shown. Vehicle vs nitroxoline, $*P = .002$, calculated using two-sided Student t test. **Error bars** = 95% confidence intervals.

Effect of Nitroxoline on the Growth of Human Breast Tumor Xenografts

Because we observed a substantial inhibitory effect of nitroxoline on angiogenesis both in vitro and in vivo, next we determined if nitroxoline had an effect on the growth of breast tumors in a mouse xenograft model. HCC1954 cells were subcutaneously transplanted into 10 female athymic nude mice (BALB/c, nu/nu-NCr), and the mice were injected either with vehicle (n = 5) or nitroxoline (n = 5) once every other day intraperitoneally for 30 days. Mice treated with nitroxoline showed statistically significantly reduced growth of HCC1954 xenografts. A 60% inhibition of tumor volume (vehicle vs nitroxoline, mean = 215.4 vs 86.5 mm³, difference = 128.9 mm³, 95% CI = 32.9 to 225.0 mm³, *P* = .012) and a 43% inhibition of tumor weight (vehicle vs nitroxoline, mean = 150.9 mg vs 86.1 mg, difference = 64.7 mg, 95% CI = 4.8 to 124.7 mg, *P* = .036) were noted on day 30 (Figure 7, A and B). To determine whether nitroxoline affected SIRT1 activity in vivo,

we performed an immunoblot analysis of the protein levels of TP53 and acetylated TP53 (acetyl-K382) in the tumor tissues (four tumors per group) on day 30. As shown in Figure 7, C, representative tumors from mice treated with nitroxoline showed a substantial increase in the level of acetylated TP53 (acetyl-K382). Consistent with the in vitro results, tumors from mice treated with nitroxoline showed an increase in the levels of TP53 (Figure 7, C), Met-14-3-3 γ , MetAP2, and RB1 proteins (Supplementary Figure 4, available online), suggesting that nitroxoline inhibited SIRT1 and MetAP2 activity in vivo.

To assess whether inhibition of tumor growth was accompanied by inhibition of angiogenesis in vivo, we performed an immunohistochemical staining of tumor tissues on day 30 using anti-CD31 antibodies, a marker of blood vessels (53), to quantitate the number of microvessels in the vehicle-treated and nitroxoline-treated tumors (Figure 7, D and E). Tumors from mice treated with nitroxoline showed a 58% inhibition of

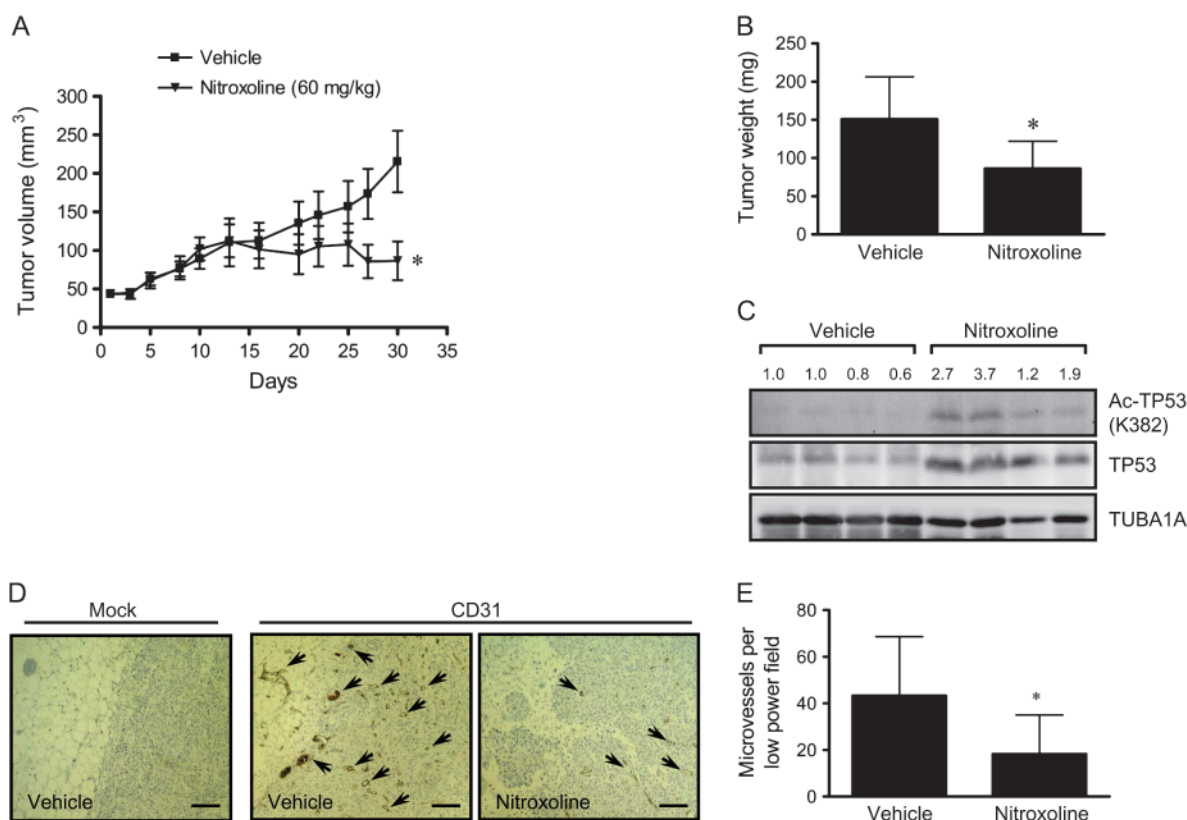


Figure 7. Effect of nitroxoline on tumor growth and angiogenesis in human breast cancer xenografts. **A)** Analysis of tumor volume. Ten female athymic nude mice (BALB/c, nu/nu-NCr) (five mice per group) bearing HCC1954 human breast cancer cells were injected intraperitoneally with vehicle or nitroxoline (60 mg/kg) every other day. Mean tumor volumes in each group are shown. Vehicle vs nitroxoline, **P* = .012, calculated by two-sided Student *t* test. **Error bars** = 95% confidence intervals. **B)** Analysis of tumor weight. Tumors were excised from mice and weighed on day 30. Mean tumor weight of five tumors from each vehicle- and nitroxoline-treated groups (five mice per group) are shown. Vehicle vs nitroxoline, **P* = .036, calculated by two-sided Student *t* test. **Error bars** = 95% confidence intervals. **C)** Immunoblot analysis of the levels of total TP53 and Ac-TP53 (acetyl-K382) in tumor samples. Tumor tissues from mice treated with either vehicle (control) or nitroxoline (60 mg/kg) were excised on day 30 and the lysates were analyzed for Ac-TP53, TP53, and tubulin, alpha 1a (TUBA1A) by

immunoblotting. TUBA1A was used as the loading control. The Ac-TP53 (acetyl-K382) levels were normalized to total TP53 protein levels and their relative differences with the control are shown. The blots are representative of three independent experiments. Ac = acetylated. **D)** Analysis of tumor microvessels by immunohistochemistry. Representative images of sections of vehicle-treated tumor stained with normal mouse immunoglobulin G antibody (mock), or vehicle- or nitroxoline-treated tumors stained with mouse anti-human CD31 antibody. Representative CD31-positive microvessels are indicated by **arrows**. Magnification $\times 100$. **Scale bar** = 200 μ m. **E)** Quantitative analysis of microvessels in the tumor tissues shown in (D) by counting four randomly selected fields in low-power (magnification $\times 100$) fields. Mean number of CD31-positive microvessels in vehicle- and nitroxoline-treated groups are shown. Vehicle vs nitroxoline, **P* = .04, calculated by two-sided Student *t* test. **Error bars** = 95% confidence intervals.

angiogenesis (CD31-positive vessels, control vs nitroxoline, mean = 43.2 vs 18.2, difference = 25, 95% CI = 1.5 to 48.4, $P = .04$) (Figure 7 E).

Effect of Nitroxoline on Tumor Growth in Mouse Orthotopic Bladder Cancer Model

Nitroxoline has been widely used in European, Asian, and African countries for treating urinary tract infections. More than 70% of nitroxoline is found in urine after oral dosing in humans as well as in mice (54). Because bladder cancer occurs within the urinary tract and its growth and metastasis are dependent on angiogenesis (55), the accumulation of nitroxoline in urine raised a possibility that it might be effective in inhibiting bladder cancer growth. To determine if nitroxoline had an effect on the growth of bladder tumors in vivo, we injected KU7-luc cells orthotopically into the

wall of mouse bladders in 11 female athymic nude mice (Hsd:Athymic Nude-*Foxn1^{nu}*). Three days after tumor cell injection, mice were given nitroxoline (30 mg/kg/day) ($n = 6$) or vehicle ($n = 5$) orally for 2 weeks, and tumor growth was detected on days 7, 11, 16, 21, and 26 using bioluminescence imaging (Figure 8, A and B). The level of toxicity, as judged by loss of body weight, showed no statistically significant difference between the vehicle- and nitroxoline-treated groups of mice (data not shown). Mice treated with nitroxoline showed a statistically significant inhibition of tumor growth compared with the vehicle-treated mice (time-course changes in tumor bioluminescence intensities of vehicle vs nitroxoline groups, $P = .045$). Histopathologic analysis of xenograft tumors showed that tumors occupied a large area of bladders in the vehicle group, but there was a substantial reduction in tumor area in the bladders of mice treated with nitroxoline (Figure 8, C).

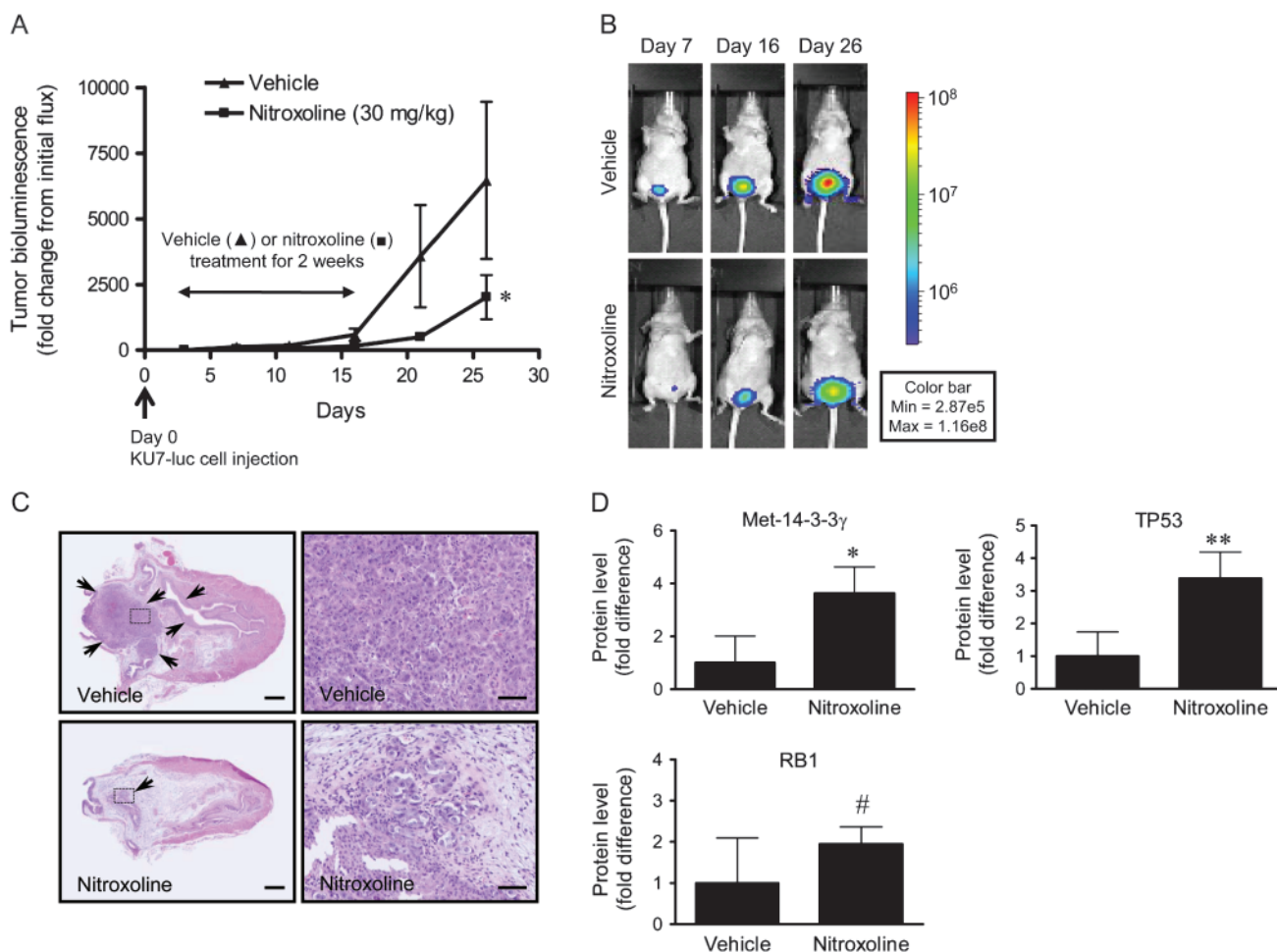


Figure 8. Effect of nitroxoline on the growth of orthotopic bladder cancer xenografts. **A)** Bioluminescence analysis. KU7 bladder cancer cells stably expressing firefly luciferase were transplanted orthotopically into the bladder of 11 female athymic nude mice (Hsd:Athymic Nude-*Foxn1^{nu}*). Mice were treated with vehicle control ($n = 5$) or nitroxoline (30 mg/kg) ($n = 6$) for 2 weeks. Mean tumor bioluminescence intensities are shown. Vehicle vs nitroxoline, $*P = .045$, calculated by two-way repeated measures analysis of variance. **B)** Bioluminescence measurement of bladder cancer growth in vehicle- and nitroxoline-treated mice on day 7, 16, and 26. Representative images are shown. **C)** Hematoxylin and eosin staining of representative bladder sections. **Arrows** indicate tumor areas in the bladder that stained more intensively compared with normal bladder cells. Whole bladder images are shown in the **left panels**

(magnification $\times 10$), and representative tumor areas (open boxes) are magnified (magnification $\times 150$) in the **right panels**. **Scale bar** = 1 mm (**left panels**) and 100 μm (**right panels**). **D)** Quantitative immunoblot analysis of methionine on 14-3-3 γ (Met-14-3-3 γ), TP53 and retinoblastoma 1 (RB1) proteins from whole bladder tissue extracts. The band intensities of the proteins in the immunoblots were quantified using ImageJ software and each protein level was normalized to the amount of glyceraldehyde 3-phosphate dehydrogenase. The mean values of fold difference in protein level in vehicle- vs nitroxoline-treated tumor tissues are shown. Fold differences in Met-14-3-3 γ protein, vehicle vs nitroxoline, $*P = .001$; for TP53 protein, vehicle vs nitroxoline, $**P < .001$; for RB1 protein, vehicle vs nitroxoline, $\#P = .025$. All P values were calculated using two-sided Student t test. **Error bars** = 95% confidence intervals.

To assess the inhibitory effect of nitroxoline on SIRT1 and MetAP2 proteins *in vivo*, bladder tissues from mice treated with vehicle or nitroxoline were subjected to immunoblot analysis. Similar to the *in vitro* results, tissues from mice treated with nitroxoline showed an increased level of Met-14-3-3 γ , TP53, and RB1 proteins (Figure 8, D). No obvious difference in SIRT1 protein level between vehicle- and nitroxoline-treated groups was observed (data not shown). The level of acetylated TP53 (acetyl-K382) in both control and nitroxoline groups could not be detected by immunoblot analysis, which prevented further analysis on TP53 (data not shown).

Discussion

In this study, we have identified the urinary tract antibiotic nitroxoline as a novel inhibitor of MetAP2 and endothelial cell proliferation from two parallel drug screens. Given the established role of MetAP2 in endothelial cell proliferation (16,17), the inhibitory effect of nitroxoline on this enzyme would have explained its inhibition of endothelial cell growth. However, a systematic comparison between the effects of nitroxoline and TNP-470, a specific MetAP2 inhibitor, at both the cellular and molecular levels, revealed substantial differences between nitroxoline and TNP-470. First, nitroxoline caused a prolonged increase in the mRNA and protein levels of p21, whereas TNP-470 induced a temporal increase in the mRNA and protein levels of p21. Second, nitroxoline induced morphological changes and premature senescence in HUVEC, whereas TNP-470 had no effect on induction of senescence. These data indicated that MetAP2 inhibition alone could not fully account for nitroxoline's effects on HUVEC, particularly on induction of premature senescence. These observations prompted us to search for other molecular targets of nitroxoline. The sirtuin family of proteins emerged as a plausible candidate based on the structural similarities between nitroxoline and some of the known inhibitors or activators of sirtuins (46). We observed that nitroxoline was a dual inhibitor of MetAP2 and sirtuins in HUVEC. Importantly, inhibition of SIRT1 was synergistic with the inhibition of MetAP2 for induction of senescence or inhibition of HUVEC proliferation, constituting a unique mechanism of action of nitroxoline in human endothelial cells. Using mouse models, we further demonstrated that nitroxoline is effective in blocking angiogenesis and cancer xenograft growth, particularly in a bladder cancer model. Given that nitroxoline has already been in use as an antibiotic to treat urinary tract infection in humans, these findings have important clinical implications for potential use of nitroxoline as a novel antiangiogenic agent.

Among the seven proteins in the human sirtuin family, SIRT1 plays an important role in longevity and cellular senescence in most organisms (24). Premature senescence occurs as a result of either aberrant expression of oncogenes or cellular stress that eventually activates the TP53 pathway by deacetylation of TP53 at K382 (45). An increase in the level of acetylated TP53 (acetyl-K382) protein accompanies the induction of premature senescence by RAS-regulated overexpression of promyelocytic leukemia (PML) protein (56). In addition, SIRT1 protein antagonizes PML-induced acetylation of TP53 protein and rescues the cells from PML-mediated premature cellular senescence (57).

These observations strongly suggest that SIRT1 regulates premature senescence through deacetylation of TP53 (acetyl-K382). Indeed, small-molecule inhibitors of SIRT1 or siRNA knock-down of SIRT1 expression have been shown to induce premature senescence in human endothelial cells by increasing the level of acetylated TP53 (26). In this study, nitroxoline strongly induced an increase in the level of acetylated TP53 (acetyl-K382) and inhibited SIRT1 activity *in vitro*. The increase in the level of acetylated TP53 (acetyl-K382) by nitroxoline was biphasic and paralleled the biphasic induction of premature senescence. The small difference in the peak concentrations of nitroxoline between TP53 acetylation (4–5 μ M) and senescence (2–4 μ M) was likely due to the difference in the drug incubation time (20 hours for TP53 acetylation vs 72 hours for senescence). These results suggest that premature senescence was induced by nitroxoline through SIRT1 inhibition and increased the level of acetylated TP53 (acetyl-K382). The molecular basis of the biphasic induction of the level of acetylated TP53 (acetyl-K382) by nitroxoline remains unclear. We also observed a biphasic induction of the level of acetylated TP53 (acetyl-K382) upon treatment of HUVEC with EX527 alone or a combination of EX527 and TNP-470, which raises a possibility that inhibition of SIRT1 activates a compensatory pathway that resulted in the decrease in the level of acetylated TP53.

Based on *in vitro* enzyme assays, nitroxoline dose-dependently inhibited the activity of both SIRT1 and SIRT2 with IC₅₀ values of 20.2 and 15.5 μ M, respectively, which was higher than that needed to induce the level of acetylated TP53 (acetyl-K382) in HUVEC (4–5 μ M). This discrepancy was likely to be due to the nitroxoline's inhibitory effect on MetAP2. Concurrent inhibition of MetAP2 and SIRT1 in HUVEC synergistically enhanced the level of acetylated TP53 (acetyl-K382), strongly suggesting that the MetAP2 and SIRT1 pathways converge upstream of TP53. The synergy between MetAP2 and SIRT1 inhibitors was not only seen at the level of acetylated TP53 (acetyl-K382) but also in inhibition of HUVEC proliferation, induction of premature senescence, and inhibition of tube formation *in vitro*. Together, these results support the notion that dual inhibition of MetAP2 and SIRT1 mediates the unique effects of nitroxoline on HUVEC. To date, however, no functional relationship between MetAP2 and SIRT1 has been reported. It will be interesting and potentially important to delineate if the MetAP2 and SIRT1 signaling pathways converge at some point and result in an increase in the level of acetylated TP53 (acetyl-K382).

As an existing clinical drug, the pharmacokinetics of nitroxoline has been extensively studied. After oral administration, nitroxoline is rapidly absorbed into the plasma within half an hour and is subsequently excreted into urine. Though a large amount of nitroxoline exists in conjugated form *in vivo*, a substantial amount of antimicrobially active free nitroxoline was found in plasma and urine (54). When administered at 5 mg/kg orally in rats, 77% of nitroxoline was eliminated from the plasma within 6 hours, whereas more than 1 μ M of free nitroxoline was still retained in the plasma for more than 10 hours. The retention time of nitroxoline in urine was even longer. When 400 mg of nitroxoline (routine use for adults: 400–750 mg/day) was administered orally to humans, as high as 10 μ M of nitroxoline was found in urine after 24 hours (54).

Based on a previous report, nitroxoline at greater than 10 μM concentration showed bacteriostatic activity and at greater than 100 μM concentrations showed bacteriocidal activity, in vitro (58). Because nitroxoline has proven to be an effective antibacterial drug in humans, the drug concentration in plasma and urinary tract administered at a dose of 400–750 mg/day must be high enough to suppress the growth of bacteria. In this study, we showed that nitroxoline inhibited HUVEC proliferation at the concentration of 1.9 μM , which is five times lower than the concentration required for bacteriostatic activity in vitro. These results suggest that nitroxoline is likely to be effective in inhibiting angiogenesis in vivo under the existing drug regimen. Thus, we used well-established mouse models to assess antiangiogenic and anticancer activities of nitroxoline in vivo. Indeed, nitroxoline statistically significantly inhibited angiogenesis and tumor growth in the breast cancer xenograft model. Given that high concentrations of nitroxoline accumulate in the urinary tract, it was tempting to speculate that it may have immediate use in the treatment of urological carcinomas such as those of the bladder. Current treatment options for superficial or early-stage bladder cancers are based on surgery with or without intravesicular chemotherapy. In this study, oral administration of nitroxoline showed promising anticancer activity against bladder cancer in the mouse orthotopic model. The targeted use of nitroxoline as an adjuvant for surgery is an intriguing possibility because 1) it showed a strong antiangiogenic activity, which, in principle, should prevent metastasis, and 2) it inhibited the growth of localized bladder cancer, which was presumably because of high accumulation of nitroxoline in urinary tract.

This study has a few limitations. We tested only a single dose of nitroxoline for in vivo mouse experiments. As nitroxoline showed biphasic induction of senescence and acetylation of TP53 in vitro, detailed dose–response effect of nitroxoline on angiogenesis and tumor growth in vivo need to be performed. In addition, the duration of treatment could be varied in the bladder cancer orthotopic xenograft model because we treated mice with nitroxoline for 2 weeks only before assessing the anticancer activity of nitroxoline, and a complete tumor remission was not achieved during this period. Another limitation is that we were not blinded to the control and treatment groups of mice, which could result in biased interpretation of results.

In conclusion, we show that nitroxoline is a novel inhibitor of angiogenesis and has a dual mechanism of action. Through inhibition of both MetAP2 and SIRT1, it increases the level of acetylated TP53, leading to the induction of premature senescence of endothelial cells. The concurrent inhibition of MetAP2 and SIRT1 is synergistic, enhancing the inhibitory effect of nitroxoline on endothelial cell proliferation and angiogenesis. The demonstration of efficacy of nitroxoline in inhibiting both angiogenesis and bladder cancer xenograft growth in vivo calls for further preclinical and clinical evaluation of nitroxoline in the treatment of bladder carcinomas.

References

1. Colville-Nash PR, Scott DL. Angiogenesis and rheumatoid arthritis: pathogenic and therapeutic implications. *Ann Rheum Dis.* 1992;51(7):919–925.
2. Ashton N. Retinal angiogenesis in the human embryo. *Br Med Bull.* 1970;26(2):103–106.

3. Folkman J, Merler E, Abernathy C, et al. Isolation of a tumor factor responsible for angiogenesis. *J Exp Med.* 1971;133(2):275–288.
4. Liekens S, De Clercq E, Neyts J. Angiogenesis: regulators and clinical applications. *Biochem Pharmacol.* 2001;61(3):253–270.
5. Folkman J. Tumor angiogenesis: therapeutic implications. *N Engl J Med.* 1971;285(21):1182–1186.
6. Folkman J, Langer R, Linhardt RJ, et al. Angiogenesis inhibition and tumor regression caused by heparin or a heparin fragment in the presence of cortisone. *Science.* 1983;221(4612):719–725.
7. Ma J, Waxman DJ. Combination of antiangiogenesis with chemotherapy for more effective cancer treatment. *Mol Cancer Ther.* 2008;7(12):3670–3684.
8. Ingber D, Fujita T, Kishimoto S, et al. Synthetic analogues of fumagillin that inhibit angiogenesis and suppress tumour growth. *Nature.* 1990;348(6301):555–557.
9. Kruger EA, Figg WD. TNP-470: an angiogenesis inhibitor in clinical development for cancer. *Expert Opin Investig Drugs.* 2000;9(6):1383–1396.
10. Bhargava P, Marshall JL, Rizvi N, et al. A Phase I and pharmacokinetic study of TNP-470 administered weekly to patients with advanced cancer. *Clin Cancer Res.* 1999;5(8):1989–1995.
11. Kudelka AP, Levy T, Verschraegen CF, et al. A phase I study of TNP-470 administered to patients with advanced squamous cell cancer of the cervix. *Clin Cancer Res.* 1997;3(9):1501–1505.
12. Twardowski P, Gradishar WJ. Clinical trials of antiangiogenic agents. *Curr Opin Oncol.* 1997;9(6):584–589.
13. Griffith EC, Su Z, Turk BE, et al. Methionine aminopeptidase (type 2) is the common target for angiogenesis inhibitors AGM-1470 and ovalicin. *Chem Biol.* 1997;4:461–471.
14. Sin N, Meng L, Wang MQW, et al. The anti-angiogenic agent fumagillin covalently binds and inhibits the methionine aminopeptidase, MetAP-2. *Proc Natl Acad Sci U S A.* 1997;94:6099–6103.
15. Bradshaw RA, Brickey WW, Walker KW. N-terminal processing: the methionine aminopeptidase and N^α-acetyl transferase families. *Trends Biochem Sci.* 1998;23:263–267.
16. Yeh JR, Mohan R, Crews CM. The antiangiogenic agent TNP-470 requires p53 and p21CIP/WAF for endothelial cell growth arrest. *Proc Natl Acad Sci U S A.* 2000;97(23):12782–12787.
17. Zhang Y, Griffith EC, Sage J, et al. Cell cycle inhibition by the anti-angiogenic agent TNP-470 is mediated by p53 and p21WAF1/CIP1. *Proc Natl Acad Sci U S A.* 2000;97(12):6427–6432.
18. Marino JP Jr., Fisher PW, Hofmann GA, et al. Highly potent inhibitors of methionine aminopeptidase-2 based on a 1,2,4-triazole pharmacophore. *J Med Chem.* 2007;50(16):3777–3785.
19. Sheppard GS, Wang J, Kawai M, et al. Discovery and optimization of anthranilic acid sulfonamides as inhibitors of methionine aminopeptidase-2: a structural basis for the reduction of albumin binding. *J Med Chem.* 2006;49(13):3832–3849.
20. Guarente L. Diverse and dynamic functions of the Sir silencing complex. *Nat Genet.* 1999;23(3):281–285.
21. Finkel T, Deng CX, Mostoslavsky R. Recent progress in the biology and physiology of sirtuins. *Nature.* 2009;460(7255):587–591.
22. Michishita E, Park JY, Burneskis JM, et al. Evolutionarily conserved and nonconserved cellular localizations and functions of human SIRT proteins. *Mol Biol Cell.* 2005;16(10):4623–4635.
23. Vaziri H, Dessain SK, Ng Eaton E, et al. hSIRT(SIRT1) functions as an NAD-dependent p53 deacetylase. *Cell.* 2001;107(2):149–159.
24. Brooks CL, Gu W. How does SIRT1 affect metabolism, senescence and cancer? *Nat Rev Cancer.* 2009;9(2):123–128.
25. Liu T, Liu PY, Marshall GM. The critical role of the class III histone deacetylase SIRT1 in cancer. *Cancer Res.* 2009;69(5):1702–1705.
26. Ota H, Akishita M, Eto M, et al. Sirt1 modulates premature senescence-like phenotype in human endothelial cells. *J Mol Cell Cardiol.* 2007;43(5):571–579.
27. Frank RG. New estimates of drug development costs. *J Health Econ.* 2003;22(2):325–330.
28. Ashburn TT, Thor KB. Drug repositioning: identifying and developing new uses for existing drugs. *Nat Rev Drug Discov.* 2004;3(8):673–683.

29. Chong CR, Chen X, Shi L, et al. A clinical drug library screen identifies astemizole as an antimalarial agent. *Nat Chem Biol.* 2006;2(8):415–6.
30. Zhang H, Qian DZ, Tan YS, et al. Digoxin and other cardiac glycosides inhibit HIF-1 α synthesis and block tumor growth. *Proc Natl Acad Sci U S A.* 2008;105(50):19579–19586.
31. Chen X, Chong CR, Shi L, et al. Inhibitors of Plasmodium falciparum methionine aminopeptidase 1b possess antimalarial activity. *Proc Natl Acad Sci U S A.* 2006;103(39):14548–14553.
32. Hadaschik BA, Black PC, Sea JC, et al. A validated mouse model for orthotopic bladder cancer using transurethral tumour inoculation and bioluminescence imaging. *BjU Int.* 2007;100(6):1377–1384.
33. Hu X, Addlagatta A, Lu J, et al. Elucidation of the function of type 1 human methionine aminopeptidase during cell cycle progression. *Proc Natl Acad Sci U S A.* 2006;103(48):18148–18153.
34. Griffith EC, Su Z, Niwayama S, et al. Molecular recognition of angiogenesis inhibitors fumagillin and ovalicin by methionine aminopeptidase 2. *Proc Natl Acad Sci U S A.* 1998;95(26):15183–15188.
35. Hu XV, Chen X, Han KC, et al. Kinetic and mutational studies of the number of interacting divalent cations required by bacterial and human methionine aminopeptidases. *Biochemistry.* 2007;46(44):12833–12843.
36. Brunet A, Sweeney LB, Sturgill JF, et al. Stress-dependent regulation of FOXO transcription factors by the SIRT1 deacetylase. *Science.* 2004;303(5666):2011–2015.
37. Ota H, Tokunaga E, Chang K, et al. Sirt1 inhibitor, Sirtinol, induces senescence-like growth arrest with attenuated Ras-MAPK signaling in human cancer cells. *Oncogene.* 2006;25(2):176–185.
38. Roy S, Packman K, Jeffrey R, et al. Histone deacetylase inhibitors differentially stabilize acetylated p53 and induce cell cycle arrest or apoptosis in prostate cancer cells. *Cell Death Differ.* 2005;12(5):482–491.
39. Solomon JM, Pasupuleti R, Xu L, et al. Inhibition of SIRT1 catalytic activity increases p53 acetylation but does not alter cell survival following DNA damage. *Mol Cell Biol.* 2006;26(1):28–38.
40. Mariadason JM, Corner GA, Augenlicht LH. Genetic reprogramming in pathways of colonic cell maturation induced by short chain fatty acids: comparison with trichostatin A, sulindac, and curcumin and implications for chemoprevention of colon cancer. *Cancer Res.* 2000;60(16):4561–4572.
41. Chou TC, Talalay P. Quantitative analysis of dose-effect relationships: the combined effects of multiple drugs or enzyme inhibitors. *Adv Enzyme Regul.* 1984;22(1):27–55.
42. Shim JS, Kim JH, Cho HY, et al. Irreversible inhibition of CD13/aminopeptidase N by the antiangiogenic agent curcumin. *Chem. Biol.* 2003;10(8):695–704.
43. Towbin H, Bair KW, DeCaprio JA, et al. Proteomics-based target identification: bengamides as a new class of methionine aminopeptidase inhibitors. *J Biol Chem.* 2003;278(52):52964–52971.
44. Sherr CJ, DePinho RA. Cellular senescence: mitotic clock or culture shock? *Cell.* 2000;102(4):407–410.
45. Toussaint O, Dumont P, Dierick JF, et al. Stress-induced premature senescence. Essence of life, evolution, stress, and aging. *Ann NY Acad Sci.* 2000;908(1):85–98.
46. Cole PA. Chemical probes for histone-modifying enzymes. *Nat Chem Biol.* 2008;4(10):590–597.
47. Liao Q, Wang J, Webster Y, et al. GPU accelerated support vector machines for mining high-throughput screening data. *J Chem Inf Model.* 2009;49(12):2718–2725.
48. North BJ, Marshall BL, Borra MT, et al. The human Sir2 ortholog, SIRT2, is an NAD⁺-dependent tubulin deacetylase. *Mol Cell.* 2003;11(2):437–444.
49. Vaquero A, Scher MB, Lee DH, et al. SirT2 is a histone deacetylase with preference for histone H4 Lys 16 during mitosis. *Genes Dev.* 2006;20(10):1256–1261.
50. Heltweg B, Gatbonton T, Schuler AD, et al. Antitumor activity of a small-molecule inhibitor of human silent information regulator 2 enzymes. *Cancer Res.* 2006;66(8):4368–4377.
51. Lain S, Hollick JJ, Campbell J, et al. Discovery, in vivo activity, and mechanism of action of a small-molecule p53 activator. *Cancer Cell.* 2008;13(5):454–463.
52. Potente M, Ghaeni L, Baldessari D, et al. SIRT1 controls endothelial angiogenic functions during vascular growth. *Genes Dev.* 2007;21(20):2644–2658.
53. Albelda SM, Muller WA, Buck CA, et al. Molecular and cellular properties of PECAM-1 (endoCAM/CD31): a novel vascular cell-cell adhesion molecule. *J Cell Biol.* 1991;114(5):1059–1068.
54. Mrhar A, Kopitar Z, Kozjek F, et al. Clinical pharmacokinetics of nitrooxoline. *Int J Clin Pharmacol Biopharm.* 1979;17(12):476–481.
55. Jaeger TM, Weidner N, Chew K, et al. Tumor angiogenesis correlates with lymph node metastases in invasive bladder cancer. *J Urol.* 1995;154(1):69–71.
56. Pearson M, Carbone R, Sebastiani C, et al. PML regulates p53 acetylation and premature senescence induced by oncogenic Ras. *Nature.* 2000;406(6792):207–210.
57. Langley E, Pearson M, Faretta M, et al. Human SIR2 deacetylates p53 and antagonizes PML/p53-induced cellular senescence. *EMBO J.* 2002;21(10):2383–2396.
58. Murugasu-Oei B, Dick T. In vitro activity of the chelating agents nitrooxoline and oxine against Mycobacterium bovis BCG. *Int J Antimicrob Agents.* 2001;18(6):579–582.

Funding

The project was funded by the Patrick C. Walsh Prostate Cancer Research Fund, National Cancer Institute, Flight Attendant Medical Research Institute, Inc, the Keck Foundation, Prostate Cancer Foundation (all to J.O.L.); and by the National Institutes of Health Medical Scientist Training Program (T32GM07309 to B.A.N.). The project was also supported in part by UL1 RR 025005 from the National Center for Research Resources, a component of the National Institutes of Health (NIH) and NIH Roadmap for Medical Research (to Johns Hopkins School of Medicine).

Notes

We are grateful to Dr Bert Vogelstein for providing HCC1954 breast cancer cell line. We thank Dr William Xu for helpful discussions and Dr Inkyu Han for helpful comments on the statistical analysis. The authors are solely responsible for the design of the study, the analysis and interpretation of the data, the writing of the manuscript, and the decision to submit the manuscript for publication.

Affiliations of authors: Department of Pharmacology and Molecular Sciences (JSS, SB, BAN, JX, HCB, KCH, CRC, MGP, JOL), Medical Scientist Training Program (BAN, CRC), Department of Radiology (SD, MGP), and Department of Oncology (JOL), Johns Hopkins School of Medicine, Baltimore, MD; The Prostate Centre at Vancouver General Hospital, University of British Columbia, Vancouver, BC, Canada (YM, AS).